Wave power extraction and coastal protection by a periodic array of oscillating buoys embedded in a breakwater

Yang Zhang[1], Xuanlie Zhao[1*], Jing Geng[1], Malin Göteman[2], Longbin Tao[3]

1. *College of Shipbuilding Engineering, Harbin Engineering University, Harbin, 150001, China*
2. *Department of Electrical Engineering, Uppsala University, Uppsala, 751 21, Sweden*
3. *Department of Naval Architecture, Ocean & Marine Engineering, University of Strathclyde, Glasgow G4 0LZ, United Kingdom*

* Corresponding author: Xuanlie Zhao, xlzhao@hrbeu.edu.cn

Abstract: The integration of wave energy devices and coastal structures may be an innovative and sustainable way to achieve energy production purposes with a secondary benefit of coastal protection, which can increase accessibility and reduce the costs of wave energy technology. In this paper, a 3-D theoretical model was developed to investigate the hydrodynamic efficiency and breakwater function of a periodic array of oscillating buoys embedded in a caisson breakwater. The generalized radiation problem was solved to derive generalized wave radiation force. The theoretical model was validated using Haskind relations and energy flux conservation law. The influences of wave /geometrical parameters and PTO damping were revealed. In particular, hydrodynamic phenomenon of multiple orders reflected and transmitted propagating waves and their influence on wave power extraction and coastal protection was examined. Results show that a satisfactory hydrodynamic efficiency and coastal defense are realized simultaneously under oblique waves for this proposed system. A decline of hydrodynamic efficiency is found beyond a critical wavenumber, accompanied by the occurrence of the strong reflection phenomenon. The findings of this paper contribute towards the preliminary design of the hybrid breakwater-WEC system for the synergy effect between the wave energy devices and breakwaters.

Keywords: wave power extraction; caisson breakwater; coastal protection; hybrid breakwater-WEC system; theoretical investigation.

This is a peer-reviewed, accepted author manuscript of the following article: Zhang, Y., Zhao, X., Geng, J., Göteman, M., & Tao, L. (2022). Wave power extraction and coastal protection by a periodic array of oscillating buoys embedded in a breakwater. Renewable Energy, 190, 434-456. https://doi.org/10.1016/j.renene.2022.03.092

1 Introduction

Ocean waves present a large reserve of renewable and environmentally friendly energy with low carbon emissions. Wave energy converters (WECs) are designed to convert the energy in ocean waves into other kinds of useful energy. WECs are separated into four categories: attenuator, oscillating water column (OWC), point absorber, and overtopping device (Falcão, 2010; Clemente et al., 2021). Most of these devices are in the stage of laboratory tests and some are in the stage of the trial/field test. Compared to other mature renewable energy technologies, wave energy is not yet economically competitive (Clément et al., 2002; López et al., 2013). For most of the designs currently developed, a single WEC will not produce significant energy so it is necessary to assemble many of them in a wave farm (Garnaud and Mei, 2009; 2010). In addition, a wave farm extracting energy from WECs can reduce the wave amplitude in the lee side, which can be served as a coastal defense measure (Abanades et al., 2014; Mendoza et al., 2014). The synergy effect of wave farms between wave power production and coastal protection enhances the economic viability of wave energy.

The higher costs and lower efficiency hinder the engineering applications of WECs (Astariz and Iglesias, 2015). A solution is to integrate WECs with coastal structures (Mustapa et al., 2017), i.e., bottom-mounded, and floating type breakwater (Zhao et al., 2019; Di Lauro et al., 2020; Zhang et al., 2020). Breakwaters can be used to mitigate wave damage and protect shorelines from erosion. The integration of WECs and breakwaters can achieve multi-function of coastal structure (i.e., both space- and cost-sharing function), further enhance accessibility and reduce costs of wave energy technology, provided with the coastal protection (Zhang et al., 2021).

For an isolated WEC, wave power extraction efficiency is significantly associated with the natural resonance of a buoy or an OWC device (Evans, 1976; Malmo and Reitan, 1985; Martins-Rivas and Mei, 2009a; 2009b). However, for the buoy array, hydrodynamic interactions of each buoy affect the efficiency significantly (Falnes and Budal, 1982; Zhao et al., 2021). Garnaud and Mei (2009; 2010) developed an analytical solution of wave scattering by an array of small heaving buoys by using the multiple-scale method. Compared to a single buoy, an array arrangement is potentially more efficient in realistic seas. Hydrodynamics of WEC array consisting of a periodically repeated single buoy or sub-array was examined by Tokić and Yue (2019). They developed a multiple scattering method and found that the presence of Bragg resonance results in a decrease in array gain. The presence of the Rayleigh resonance was verified for the truncated cylinder array. Zheng et al. (2019) developed a

theoretical model to evaluate hydrodynamics of multiple OWCs installed along a straight coast. They pointed out that the observed enhancement of efficiency is attributed to the wave reflection of the coastal wall and the positive effect caused by the constructive interactions of an OWC array (Göteman et al., 2018). Compared to an isolated device, the WEC array can enhance the wave energy absorption, and efficiency is significantly influenced by the array phenomena, such as wave interference or Bragg resonance.

Oblique or directional waves occur frequently in realistic sea states, and the assessment of the wave power extraction performance is essential for WECs or breakwater (Tay and Venugopal, 2019). Many investigations were conducted to explore oblique wave interactions with bottom-mounted structures (Teng et al., 2004; Liu et al., 2007; Jalón et al., 2019). The case of the ordinary heaving problem was studied by Ursell (l949). Then, Bolton and Ursell (1973) proposed a generalized heaving problem of an infinitely long circular cylinder to derive the generalized vertical force, on the assumption of a flexural wave traveling along the surface of the cylinder and generating an oblique wave (Sannasiraj et al., 2001; Politis et al., 2002). Considering the cartesian coordinate of an infinite long floating rectangle structure, Zheng et al. (2006; 2007) analytically investigated the generalized radiation force in cases of oblique waves under the context of the linear potential flow theory. This wave radiation was not due to the forced motions of the structure under the normal incidence (Abul-Azm and Gesraha, 2000), which fails Haskind relations. The corresponding governing equation is a two-dimensional modified Helmholtz equation. The agreement of wave force between calculation from the incident and radiated potentials and results from diffracted potentials can be realized. This solution can be also referred to in the numerical investigation (Islam et al., 2019). It is worth noting that, due to the consideration of the incident wave direction, the radiation problem of the floating structures can be named generalized radiation problem (GRP). Specifically, the eigenfunction expression of the GRP involves the term of incident wave angle θ. Hence, there is a significant correlation between generalized hydrodynamic coefficients (i.e., added mass and radiation damping) calculated by solving GRP and the direction of radiated waves. This GRP is different from an isolated/array cylinder structure (i.e., truncated cylinder, OWC, etc.) (Siddorn and Eatock Taylor, 2008; Wolgamot et al., 2015; Zheng et al., 2019). Therefore, the previous works related to GRP concern an infinite long rectangle structure. However, wave farm consists of many WECs with gaps perpendicular or along with incident waves. The solution of GRP by an infinite array of floating structures is limited.

The present study analyzed the hydrodynamic performance of oscillating-buoy WECs integrated with bottom-mounted caisson breakwater consisting of a periodic array of separated caissons under the oblique waves. As for caisson array with gaps, this structure is similar to the diffraction gratings in the optical field (Strutt, 1907). According to the scattering theory for diffraction gratings, there exists the phenomenon of Wood anomaly (Wilcox, 1984; Wood, 1901), which represents a rapid or discontinuous change in parameters as propagation modes are on or off. Especially, the first type of anomalies occurs at the wavelengths at which a diffracted order appears or disappears at a grazing angle, which is called Rayleigh wavelength (Bloch, 1929; Maradudin et al., 2016). Under the context of the water wave, multiple reflected/transmitted propagating waves triggered by a periodic array of caissons or barriers separated by gaps were found (Dalrymple and Martin, 1990; Fernyhough and Evans, 1995; Linton and McIver, 2001; Wang et al., 2019), but only involving scattering problem, which significantly affects wave attenuation performance and the total wave force of breakwater. Zhao et al. (2020; 2021) investigated the hydrodynamic performance of the integration of heaving buoy devices and caisson breakwater separated by gaps in the normal incident waves. They mainly revealed that the wave energy gathering effect caused by adjacent caissons and the flange is beneficial for an increment of efficiency of the WEC. But the array configuration and oblique waves were not considered for this hybrid breakwater-WEC system, with a focus on the hydrodynamic efficiency and coastal defense.

In the present study, we systematically investigated the hydrodynamic interaction of the breakwater and the wave energy devices array under the normal and oblique waves. A 3-D theoretical model of oblique waves interacting with a periodic array of caisson breakwater equipped with oscillating-buoy WECs was developed, using the eigenfunction matching method, based on the linear potential flow theory. The solutions of the wave scattering problem and GRP were examined by using Haskind relations and wave energy flux conservation rule. The influence of wave parameters (i.e., incidence angle), geometrical parameters, and PTO damping on wave power extraction and coastal protection was revealed.

2 Mathematical model

As is shown in Fig 1a, the hybrid breakwater-WEC system considered here consists of caissons and a periodic of heaving oscillating buoys with the linear power take-off (PTO). The breakwater is considered as a base structure. Oscillating buoys working in the principle of heaving-type WEC are

located between the adjacent caissons.-Symbolically, $2w_1$ and $2B$ denote the width and breadth of the caisson, respectively. $2w_2$ and $2b_2$ are the width and breadth of a buoy. The draft of the buoy and flange are d_1 and d_2. The position of the buoy is determined by $2b_1$ and $2b_3$, which represent the spacing between the buoy and caisson wall. A global cartesian coordinate system o-xyz is employed in the model, and the origin of o is located at the cross-point of the medial axis of the buoy and still water surface. The z- and the y-axis are positive in the vertically upward direction and along with a breakwater. The symbols A, L, k, T, h and θ_0 ($0 \le \theta_0 < \pi/2$) represent wave amplitude, wavelength, wavenumber, period, water depth, and incident angle, respectively. The wavenumber k is determined by the dispersion relation $\omega^2 = gk\tanh(kh)$. The component of wavenumber in x- and y-direction corresponds to $k_x = k\cos\theta_0$ and $k_y = k\sin\theta_0$, respectively. For convenience, following notes are as follow: $l = w_1 + w_2$, $r_1 = b_1 + b_2$, $r_2 = 2b_1 + b_2$, $r_3 = b_2 + b_3$ and $r_4 = b_2 + 2b_3$.

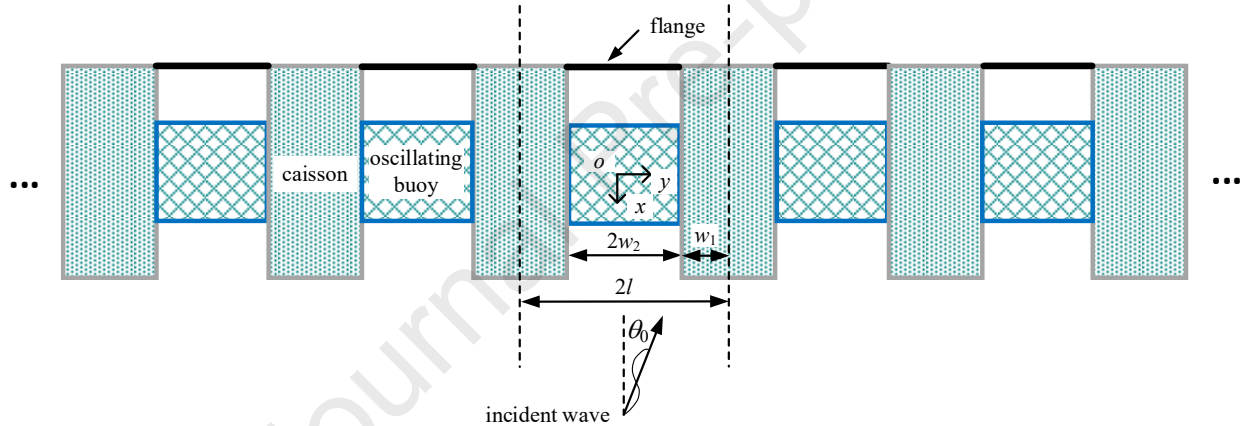

(a) top view (array)

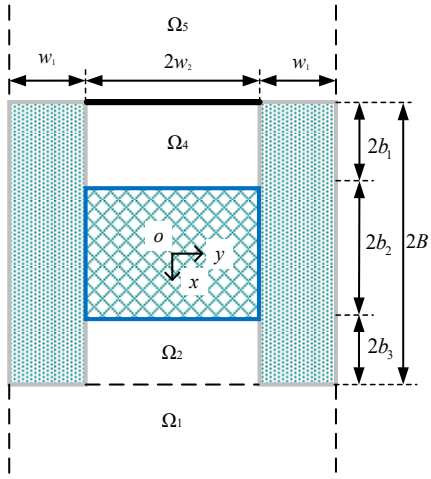

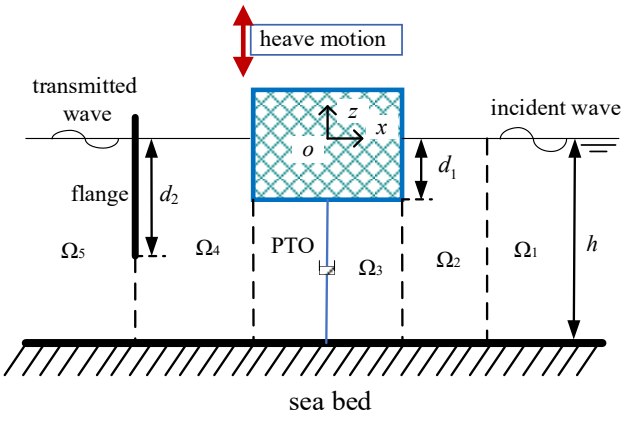

(b) top view of a unit (c) section view of the buoy and the flange

Fig. 1. The sketch of the hybrid breakwater-WEC system.

We consider the case of small wave steepness ($kA \ll 1$) and small amplitude of buoy motion, so the

system can be studied in the framework of linear potential flow theory. The velocity potential $\Phi(x, y, z, t)$ can be used to describe the wave motion problem, and the time factor $e^{-i\omega t}$ can be factored out as

$$\Phi(x,y,z,t) = \mathrm{Re}\left[\phi(x,y,z)e^{-i\omega t}\right], \tag{1}$$

where $\phi(x, y, z)$ is a complex spatial velocity potential independent of time t, Re[ ]denotes the real part of the variables, ω represents the angular frequency and i denotes imaginary unit. The complex spatial velocity potential $\phi(x, y, z)$ satisfies 3-D Laplace equation $\nabla^2\phi = 0$ (∇^2 is Laplace operator). Due to the linearity, the velocity potential can be decomposed as the sum of scattering and radiation potentials $\phi = \phi_S + \phi_R$, where ϕ_S and ϕ_R are the scattering and radiation potential, respectively.

2.1 Scattering problem

The geometry features of this system present a periodicity $2l$. The scattering potential in the regions satisfies the periodicity condition (Linton and McIver, 2001; Nazarov and Videman, 2010):

$$\phi_S(x, y+2l, z) = e^{i2lk_y}\phi_S(x, y, z). \tag{2}$$

Therefore, the fluid field can be determined by the scattering potential in the fluid domain of $\{-\infty < x < \infty, -l \le y \le l \text{ and } -h \le z \le 0\}$. The fluid domain is divided into five subdomains, which are defined by Ω_i ($i = 1 \sim 5$) shown in Fig. 1b and 1c. Correspondingly, the scattering potential in each subdomain is denoted by $\phi_S^{(i)}$ ($i = 1 \sim 5$), which satisfies the non-penetration condition of all rigid boundaries (including seabed, caisson, flange, and a buoy), as well as the linearized free surface boundary condition. The boundary conditions for the scattering problem refer to Eqs. (A.1) - (A.7). Besides, velocity potentials must satisfy the far-field radiation conditions. By using the matching eigenfunction expansion method, the scattering potentials $\phi_S^{(i)}$ ($i = 1 \sim 5$) can be expressed as

$$\phi_S^{(1)} = -\frac{igA}{\omega}\left\{e^{-ik_x(x-r_4)}e^{ik_y y}Z_0(z) + \sum_{i=-\infty}^{+\infty}E_i(y)\sum_{n=0}^{+\infty}A_{i,n}e^{p_{i,n}(x-r_4)}Z_n(z)\right\}, \tag{3}$$

$$\phi_S^{(2)} = -\frac{igA}{\omega}\left\{\sum_{j=0}^{+\infty}\bar{C}_j(y)\sum_{n=0}^{+\infty}\left(B_{j,n}\frac{\cosh\left[\bar{p}_{j,n}(x-r_3)\right]}{\cosh\left[\bar{p}_{j,n}b_3\right]} + C_{j,n}\frac{\sinh\left[\bar{p}_{j,n}(x-r_3)\right]}{\sinh\left[\bar{p}_{j,n}b_3\right]}\right)Z_n(z)\right\}, \tag{4}$$

$$\phi_S^{(3)} = -\frac{igA}{\omega}\left\{\begin{array}{l}\left(D_{0,0} + E_{0,0}\dfrac{x}{b_2}\right) + \displaystyle\sum_{n=1}^{+\infty}\left(D_{0,n}\frac{\cosh\left(q_{0,n}x\right)}{\cosh\left(q_{0,n}b_2\right)} + E_{0,n}\frac{\sinh\left(q_{0,n}x\right)}{\sinh\left(q_{0,n}b_2\right)}\right)\varphi_n(z) \\ + \displaystyle\sum_{j=1}^{+\infty}\bar{C}_j(y)\sum_{n=0}^{+\infty}\left(D_{j,n}\frac{\cosh\left(q_{j,n}x\right)}{\cosh\left(q_{j,n}b_2\right)} + E_{j,n}\frac{\sinh\left(q_{j,n}x\right)}{\sinh\left(q_{j,n}b_2\right)}\right)\varphi_n(z)\end{array}\right\}, \tag{5}$$

$$\phi_S^{(4)} = -\frac{\mathrm{i}gA}{\omega}\left\{\sum_{j=0}^{+\infty}\bar{C}_j(y)\sum_{n=0}^{+\infty}\left(F_{j,n}\frac{\cosh\left[\bar{p}_{j,n}(x+r_1)\right]}{\cosh\left[\bar{p}_{j,n}b_1\right]}+G_{j,n}\frac{\sinh\left[\bar{p}_{j,n}(x+r_1)\right]}{\sinh\left[\bar{p}_{j,n}b_1\right]}\right)Z_n(z)\right\}, \tag{6}$$

$$\phi_S^{(5)} = -\frac{\mathrm{i}gA}{\omega}\left\{\sum_{i=-\infty}^{+\infty}E_i(y)\sum_{n=0}^{+\infty}H_{i,n}\mathrm{e}^{-p_{i,n}(x+r_2)}Z_n(z)\right\}, \tag{7}$$

where g is the acceleration due to gravity. The vertical eigenfunctions of $Z_n(z)$ and $\varphi_n(z)$ can be expressed as

$$Z_n(z) = \frac{\cos\left[k_n(z+h)\right]}{\cos\left[k_n h\right]} \tag{8}$$

and

$$\varphi_n(z) = \cos\left[\mu_n(z+h)\right], \tag{9}$$

with eigenvalues of $\mu_n = n\pi/(h-d_1)$, $n = 0, 1, 2, \ldots$. $k_0 = -\mathrm{i}k$ and k_n ($n \geq 1$) satisfying the equation of $\omega^2 = -gk_n\tan(k_n h)$. The y-direction eigenfunctions of $E_i(y)$ and $\bar{C}_j(y)$ can be expressed as

$$E_i(y) = \mathrm{e}^{\mathrm{i}\gamma_i y}, \tag{10}$$

with eigenvalues of $\gamma_i = k_y + i\pi/l$ ($i = \ldots, -2, -1, 0, 1, 2, \ldots$) and

$$\bar{C}_j(y) = \cos\left[\bar{\gamma}_j(w_2 - y)\right], \tag{11}$$

with eigenvalues of $\bar{\gamma}_j = j\pi/(2w_2)$ ($j = 0, 1, 2, \ldots$). $p_{i,n}$, $\bar{p}_{j,n}$ and $q_{j,n}$ are defined for convenience and are specified in Eqs. (A.8) - (A.10) in Appendix A. Keep in mind that the first part in Eq. (3) represents the incident velocity potential ϕ_I with an angular frequency of ω and wave amplitude of A. Besides, $A_{i,n}$, $B_{j,n}$, $C_{j,n}$, $D_{j,n}$, $E_{j,n}$, $F_{j,n}$, $G_{j,n}$ and $H_{i,n}$ are the unknowns to be solved.

2.2 Generalized radiation problem

Upon the assumption of the small motion amplitude, the radiation potential $\phi_R(x, y, z)$ can be written as $-\mathrm{i}\omega\chi\varphi(x, y, z)$, where χ represents the amplitude of forced heave motion. $\varphi(x, y, z)$ indicates the radiation potential independent of the motion amplitude and frequency. Recalling the divisions of the fluid domain described above, we introduce the symbol $\varphi_R^{(i)}$ to represent the radiation potential in the domain of Ω_i ($i = 1 \sim 5$).

The boundary conditions of GRP resemble Eqs. (A.1) - (A.7), except for the heaving oscillating buoy bottom condition. By implementation of the separation variables method, generalized radiation velocity potentials in the different fluid regions can be written as a product of eigenfunctions as

$$\varphi_R^{(1)} = -\frac{\mathrm{i}gA}{\omega}\left\{\sum_{i=-\infty}^{+\infty} E_i(y)\sum_{n=0}^{+\infty} A'_{i,n}\mathrm{e}^{p_{i,n}(x-r_4)}Z_n(z)\right\}, \tag{12}$$

$$\varphi_R^{(2)} = -\frac{\mathrm{i}gA}{\omega}\left\{\sum_{j=0}^{+\infty} \bar{C}_j(y)\sum_{n=0}^{+\infty}\left(B'_{j,n}\frac{\cosh\left[\bar{p}_{j,n}(x-r_3)\right]}{\cosh\left[\bar{p}_{j,n}b_3\right]} + C'_{j,n}\frac{\sinh\left[\bar{p}_{j,n}(x-r_3)\right]}{\sinh\left[\bar{p}_{j,n}b_3\right]}\right)Z_n(z)\right\}, \tag{13}$$

$$\varphi_R^{(3)} = -\frac{\mathrm{i}gA}{\omega}\left\{\begin{array}{l}\left(D'_{0,0} + E'_{0,0}\dfrac{x}{b_2}\right) + \displaystyle\sum_{n=1}^{+\infty}\left(D'_{0,n}\frac{\cosh\left(q_{0,n}x\right)}{\cosh\left(q_{0,n}b_2\right)} + E'_{0,n}\frac{\sinh\left(q_{0,n}x\right)}{\sinh\left(q_{0,n}b_2\right)}\right)\varphi_n(z) \\ + \displaystyle\sum_{j=1}^{+\infty}\bar{C}_j(y)\sum_{n=0}^{+\infty}\left(D'_{j,n}\frac{\cosh\left(q_{j,n}x\right)}{\cosh\left(q_{j,n}b_2\right)} + E'_{j,n}\frac{\sinh\left(q_{j,n}x\right)}{\sinh\left(q_{j,n}b_2\right)}\right)\varphi_n(z)\end{array}\right\} + \frac{(z+h)^2 - x^2}{2(h-d_1)}, \tag{14}$$

$$\varphi_R^{(4)} = -\frac{\mathrm{i}gA}{\omega}\left\{\sum_{j=0}^{+\infty} \bar{C}_j(y)\sum_{n=0}^{+\infty}\left(F'_{j,n}\frac{\cosh\left[\bar{p}_{j,n}(x+r_1)\right]}{\cosh\left[\bar{p}_{j,n}b_1\right]} + G'_{j,n}\frac{\sinh\left[\bar{p}_{j,n}(x+r_1)\right]}{\sinh\left[\bar{p}_{j,n}b_1\right]}\right)Z_n(z)\right\}, \tag{15}$$

$$\varphi_R^{(5)} = -\frac{\mathrm{i}gA}{\omega}\left\{\sum_{i=-\infty}^{+\infty} E_i(y)\sum_{n=0}^{+\infty} H'_{i,n}\mathrm{e}^{-p_{i,n}(x+r_2)}Z_n(z)\right\}. \tag{16}$$

Compared with the condition of normal incidence angle (Zhao et al., 2020; 2021), the difference of radiation potential expressions is *y*-direction eigenfunction in Eqs. (12) and (16). Therefore, for the wave radiation problem of a periodic of oscillating buoys, flexural waves travel perpendicular to normal incident waves, out of the system (i.e., Ω_1 and Ω_5), instead of the surface of the buoy (Zheng et al., 2006; 2007). This is due to the non-penetration condition of the caisson in Ω_2 and Ω_4. Different from GRP of an infinite long buoy, the periodicity of the oscillating buoy array should be taken into consideration. A flexural wave with array periodicity of the *y*-direction component is generated for this system. This assumption of GRP can be induced the ordinary radiation problem under the $\theta_0 = 0$.

2.3 Solution procedures

There exists a strong singularity at the sharp edge of the flange, the convergence of the solutions with increasing truncation cut-off was found rather slow (Evans and Porter, 1995; He et al., 2019). Also, the Galerkin approximation method was already applied to analytically solve the hydrodynamic problem of water wave interaction with sharp corners of WECs (Renzi and Dias, 2012; Renzi and Dias, 2013; Renzi et al., 2014). The Galerkin approximation method proposed by Evans and Porter (1995) was adopted to handle the velocity singularity at the edge of the flange, which is identical to Zhao et al. (2021). The detailed description can be found in Appendix A.

To solve the unknown coefficients in Eqs. (3) - (7) and (12) - (16), we require that the potentials and their derivates (i.e., the pressure and velocity) are continuous at the interface of two neighboring

fluid domains. The continuities are summarized explicitly in Eqs. (A.11) - (A.19).

By inserting the expressions of scattering and radiated velocity potentials Eqs. (3) - (7) and (12) - (16) into the continuity conditions and utilizing the orthogonal relations of eigenfunctions Eqs. (8) - (11), a system of linear equations is formed by truncating the infinite series of velocity potentials. Specifically, the symbols of *i, j*, *n* and *q* in velocity potential expressions and auxiliary function of Eq. (A.20) are truncated from -*M* to *M,* 0 to *M*, 0 to *N,* and 0 to *Q*. The unknown coefficients of the scattering or radiated problem with a size of $(10M+Q+9)(N+1)$ are calculated. Hence, the scattering or radiated velocity potential for each fluid region is determined. The detailed matrix information of the linear equations can be referred to in Eqs. (B.1) - (B.42).

2.4 Wave power extraction

Based on the linear Bernoulli equation, the generalized wave excitation force in heave mode F_z can be calculated as the integral of the scattering potential over the wetted bottom surface of the buoy

$$F_z = \mathrm{i}\omega\rho\iint_{S_b}\phi_S^{(3)}\vec{n}_z \mathrm{d}S\,, \tag{17}$$

where ρ denotes water density and $\vec{n}_z$ is the unit normal vector pointing to the buoy along with the positive *z*-axis direction. Similarly, the generalized heaving radiation force can be obtained by the integral of the radiation potential

$$F_z^{(1)} = \mathrm{i}\omega\rho\iint_{S_b}\phi_R^{(3)}\vec{n}_z \mathrm{d}S = \omega^2\mu + \mathrm{i}\omega\lambda\,, \tag{18}$$

where μ and λ represent added mass and radiated damping of a heaving oscillating buoy, respectively. By the implementation of the linear PTO damping λ_{PTO}, the frequency-domain heaving motion equation can be written as

$$\xi = \frac{F_z}{K-\omega^2\left(M+\mu\right)-\mathrm{i}\omega\left(\lambda+\lambda_{\mathrm{PTO}}\right)}, \tag{19}$$

where $K = 4w_2b_2\rho g$ and $M = 4w_2b_2\rho d_1$ are the restoring stiffness term and the mass term of a buoy, respectively, and ξ denotes the heaving motion amplitude. Once ξ is obtained, the heave response amplitude operator (HRAO) can be expressed as ξ/A, and the absorbed power P_{c} of a buoy can be calculated as

$$P_{\mathrm{c}} = \frac{1}{2}\lambda_{\mathrm{PTO}}\omega^2\left|\xi\right|^2. \tag{20}$$

Correspondingly, the optimal PTO damping of an isolated buoy-WEC can be expressed as

$$\lambda_{\text{optimal}} = \sqrt{\left[K/\omega - \omega\left(M+\mu\right)\right]^2 + \lambda^2}\ . \tag{21}$$

The hydrodynamic efficiency is calculated as $\eta = P_c/P_i$, where the incident wave power P_i at the unit system width of $2l$ can be expressed as

$$P_i = \frac{\rho g A^2 \omega l}{2k}\left(1+\frac{2kh}{\sinh 2kh}\right)\cos\theta_0\ . \tag{22}$$

2.5 Reflection and transmission coefficients

The reflection and transmission coefficients are key to evaluating the performance of breakwaters. In addition, wave transmission is associated significantly with coastal defense. Based on the scattering theory of diffraction gratings (Wilcox, 1984), the reflected or transmitted waves from a periodic array involve several modes propagating waves, traveling in different directions. For the proposed system, the multiple orders propagating waves due to GRP are also involved. Specifically, the total number of reflected/transmitted propagating waves is $M_1 + M_2 + 1$, where M_1 and M_2 can be expressed by

$$M_1 = \text{int}\left[\left(1+\sin\theta_0\right)kl/\pi\right] \tag{23}$$

and

$$M_2 = \text{int}\left[\left(1-\sin\theta_0\right)kl/\pi\right], \tag{24}$$

where the floor function of int[ ] represents the integer part of variables in the square bracket. Here, m-th order reflected propagating waves travel in the direction of θ_m (m = -M_1, …, 0, …, M_2). The traveling direction of the corresponding mode transmitted propagating waves is $\pi - \theta_m$. θ_m can be determined by the grating equation of

$$\sin\theta_m = \left|\sin\theta_0 + m\pi/\left(kl\right)\right|. \tag{25}$$

Furthermore, the energy flux per meter crest width over a wave period is expressed for the incident wave J^{I}, m-th order reflected propagating wave $\mathrm{J}^{\mathrm{R}}_{(m)}$, and m-th order transmitted propagating wave $\mathrm{J}^{\mathrm{T}}_{(m)}$ in the x-directions as

$$\mathrm{J}^{\mathrm{I}} = \frac{1}{2}\rho g A^2 C_g \cos\theta_0\,, \tag{26}$$

$$\mathrm{J}^{\mathrm{R}}_{(m)} = \frac{1}{2}\rho g\left[A\left|A_{m,0} - \mathrm{i}\omega\zeta A'_{m,0}\right|\right]^2 C_g\cos\theta_m \tag{27}$$

and

$$\mathrm{J}_{(m)}^{\mathrm{T}}=\frac{1}{2}\rho g\left[A\left|H_{m,0}-\mathrm{i}\omega\zeta H'_{m,0}\right|\right]^2 C_g\cos\theta_m,$$

respectively. (28)

Here, the wave group velocity of C_g is expressed as

$$C_g=\frac{\omega}{2k}\left(1+\frac{2kh}{\sinh\left[2kh\right]}\right). \tag{29}$$

Therefore, m-th order reflection coefficient $K_{\mathrm{R}}^{(m)}$ and m-th order transmission coefficient $K_{\mathrm{T}}^{(m)}$ are defined as

$$K_{\mathrm{R}}^{(m)}=\sqrt{\frac{\mathrm{J}_{(m)}^{\mathrm{R}}}{\mathrm{J}^{\mathrm{I}}}}=\left|A_{m,0}-\mathrm{i}\omega\zeta A'_{m,0}\right|\sqrt{\frac{\sqrt{1-\left[\sin\theta_0+m\pi/(kl)\right]^2}}{\cos\theta_0}} \tag{30}$$

and

$$K_{\mathrm{T}}^{(m)}=\sqrt{\frac{\mathrm{J}_{(m)}^{\mathrm{T}}}{\mathrm{J}^{\mathrm{I}}}}=\left|H_{m,0}-\mathrm{i}\omega\zeta H'_{m,0}\right|\sqrt{\frac{\sqrt{1-\left[\sin\theta_0+m\pi/(kl)\right]^2}}{\cos\theta_0}}, \tag{31}$$

respectively.

The total wave reflection coefficient K_{R} and transmission coefficient K_{T} are defined as the square root of the ratio of the energy flux of sum reflected and transmitted waves and the incident wave energy flux, respectively. The detailed expressions are drawn as

$$K_{\mathrm{R}}=\sqrt{\frac{\sum_{m=-M_1}^{M_2}\mathrm{J}_{(m)}^{\mathrm{R}}}{\mathrm{J}^{\mathrm{I}}}}=\sqrt{\frac{\sum_{m=-M_1}^{M_2}\left|A_{m,0}-\mathrm{i}\omega\xi A'_{m,0}\right|^2\sqrt{1-\left[\sin\theta_0+m\pi/(kl)\right]^2}}{\cos\theta_0}} \tag{32}$$

and

$$K_{\mathrm{T}}=\sqrt{\frac{\sum_{m=-M_1}^{M_2}\mathrm{J}_{(m)}^{\mathrm{T}}}{\mathrm{J}^{\mathrm{I}}}}=\sqrt{\frac{\sum_{m=-M_1}^{M_2}\left|H_{m0}-\mathrm{i}\omega\xi H'_{m0}\right|^2\sqrt{1-\left[\sin\theta_0+m\pi/(kl)\right]^2}}{\cos\theta_0}}. \tag{33}$$

In the higher-frequency region, the M_1 or M_2 may be greater than 1 (Eq. (23) and (24)). Compared with cases of the lower frequency region, the reflected and transmitted waves involve more mode propagating waves traveling in different directions, which satisfy the conditions of $kl = |m\pi/[(1 \pm \sin\theta_0)]|$ (a similar trigger condition was also found in Wang et al. (2019)). The trigger condition is identical to that of Wood anomaly (Wilcox, 1984), but includes the condition of GRP for the present model. Physically, the contributions caused by the appearance of the multiple orders propagation waves shall be involved in an increment or a reduction of reflection and transmission coefficients. This would affect the wave power extraction performance significantly, as well as wave attenuation

performance or coastal protection.

3 Model validations

3.1 Convergence analysis

Firstly, we analyze how many terms in the infinite sums in the velocity potentials expressions must be used to reach the convergence of the solution, i.e., we identify the required truncation cut-off. The truncated numbers M (N and Q) vary when the other two truncated numbers are fixed. Geometrical and wave parameters are set for $d_1/h = 1/6$, $l/h = 5/6$, $w_1/l = 1/5$, $b_2/h = 1/2$, $b_1/b_2 = b_3/b_1 = 1/3$, $d_2/h = 1/6$, $\theta_0 = \pi/6$ and the optimal PTO damping λ_{PTO}. It is found that a sufficient convergence was obtained when truncating the infinite sums to $M = 15$, $N = 25$, and $Q = 5$.

2.2 Haskind's relations

Given ordinary radiation problem, the wave exciting force calculated by the radiation and incident potential do not agree with that derived by the diffraction potential under oblique waves (Zheng et al., 2006). Based on the solution of GRP in the present study, the generalized wave exciting force acting on the bottom of the oscillating buoy is also calculated by radiated and incident velocity potentials. Based on Haskind's relationship (Falnes and Kurniawan, 2020), the wave exciting force can be also written as

$$F_z^{(\mathrm{R})} = -\mathrm{i}\omega\rho\iint_{S_\infty}\left(\phi_{\mathrm{I}}\frac{\partial\phi_R}{\partial\vec{n}} - \phi_R\frac{\partial\phi_{\mathrm{I}}}{\partial\vec{n}}\right)\mathrm{d}S = 4\rho g l A^2\left|A'_{0,0}\right|\cos\theta_0 C_g\,. \tag{34}$$

where $\vec{n} = (\vec{n}_x, \vec{n}_y, \vec{n}_z)$ denotes the unit normal vector along x-, y- and z-direction. Fig. 2 plots results of $F_z^{(\mathrm{R})}$ and F_z for parameters of $d_1/h = d_2/h = 1/6$, $l/h = 1/2$, $w_1/l = w_2/l = 1/2$, $B/h = 1$, $b_1/B = b_2/B = b_3/B = 1/3$. It can be found that an overall agreement can be achieved, which verifies the solution of GRP for a periodic array of oscillating buoys.

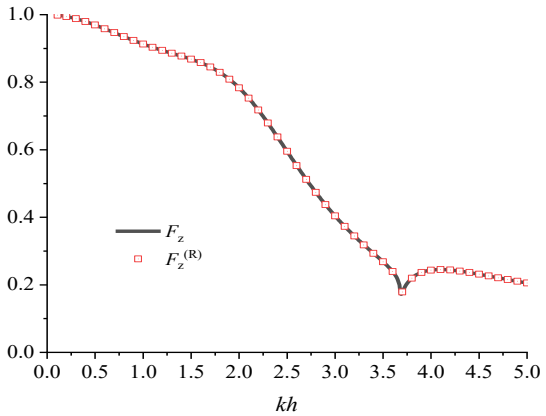

Fig. 2. Comparisons of results between F_z and $F_z^{(\mathrm{R})}$.

3.3 Energy flux conservation law

Energy flux conservation law implies that the waves are either reflected, transmitted, or absorbed, which in the framework of potential flow theory can be expressed as $K_R^2 + K_T^2 + \eta = 1$. Fig. 3 shows the results of K_R, K_T, η and $K_R^2 + K_T^2 + \eta$ for the case in Section 3.2. The PTO damping is selected as the optimal PTO damping. As shown in Fig. 3, the energy flux conservation is satisfied, which serves as a verification of the present analytical model.

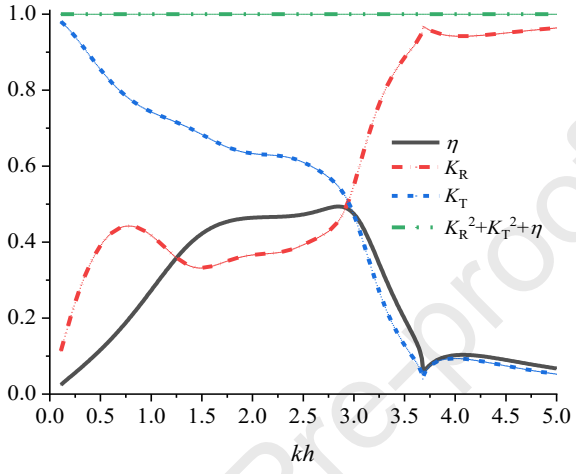

Fig. 3. Variations of the K_R, K_T, η and $K_R^2 + K_T^2 + \eta$ versus the dimensionless wavenumber kh.

4 Results and discussions

4.1 Effect of incident wave direction

Results of hydrodynamic efficiency η, transmission coefficients K_T, reflection coefficients K_R, the generalized wave excitation force $F_z/(4\rho g A b_2 w_2)$, added mass $\mu/(4\rho b_2 w_2 d_1)$, radiation damping $\lambda/(4\rho\omega b_2 w_2 d_1)$ and HRAO are shown in Fig. 4. The geometrical parameters are $d_1/h = 1/6$, $l/h = 5/6$, $w_1/l = 2/5$, $w_2/l = 3/5$, $b_2/l = 1/2$, $B/l = 9/10$, $b_1/l = b_3/l$ and $d_2/h = 1/6$. The effect of incident wave angles is revealed by considering six incidence wave angles of $\theta_0 = 0$, $\pi/12$, $\pi/6$, $\pi/4$, $\pi/3$, and $5\pi/12$. In the frequency region $0 \le kh \le 1.75$, η for different incident angles (in exception of $5\pi/12$) increases to the first peak of 0.5 roughly with increasing dimensionless wavenumber kh. For the condition of normal incident waves $\theta_0 = 0$, η exhibits two peak values ($kB = 0.416\pi$ and 0.851π), due to multiple wave resonances inside the wave chamber (Zhao et al., 2020). Considering the absence of an oscillating buoy, the system is simplified as the caisson array. The case of zeros reflection $K_R = 0$ is triggered by $kB \approx 0.5n\pi$ (Zhu et al., 2017), but the influences of geometry on the occurrence of phase downward shift are not neglected. An incident wavelength longer than the original wavelength is required to compensate for the phase loss of reflected waves by the superposition of waves with

opposite directions. Therefore, the appearance of this phenomenon is $kB < 0.5n\pi$. η increases successively for the region of $0 \le kh \le 1.5$, and K_R has a successive decreasing trend. HRAO decreases at $0 \le kh \le 1.5$ with an increase in the incident angle. Interestingly, η exhibits an abrupt change for different incident angles in the whole frequency domain, as shown in Table 1.

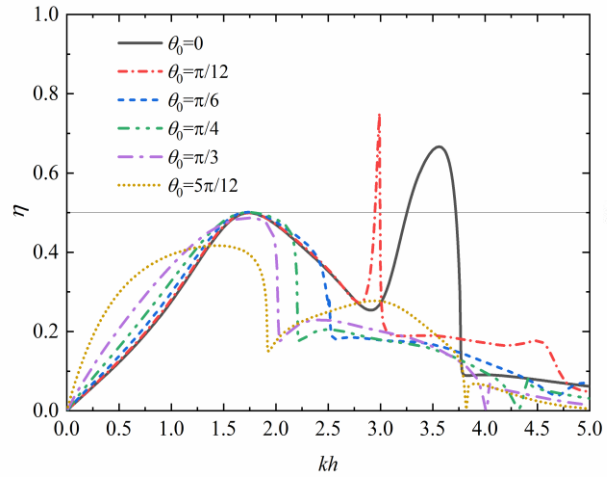

(a) η

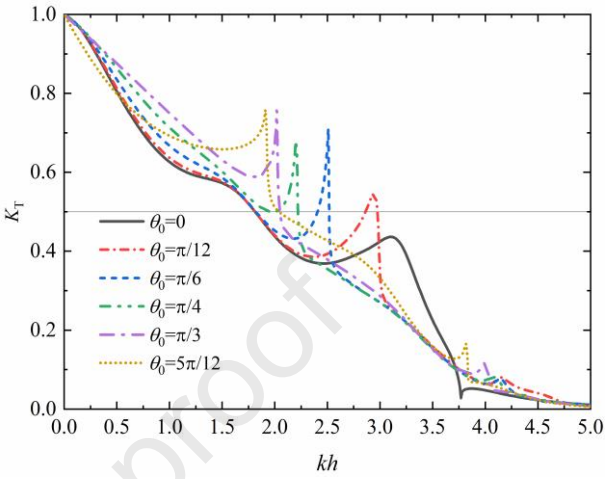

(b) K_T

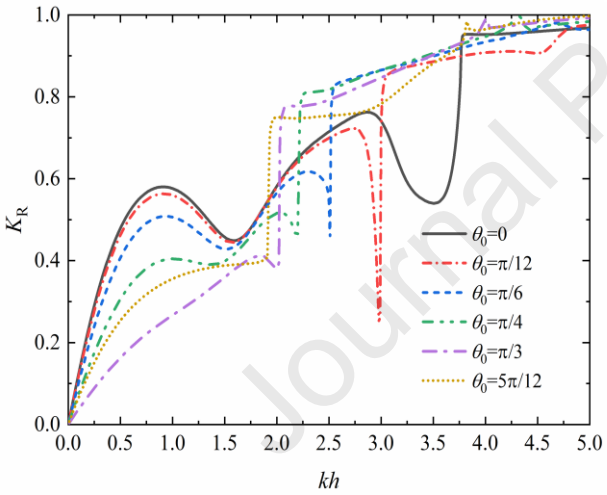

(c) K_R

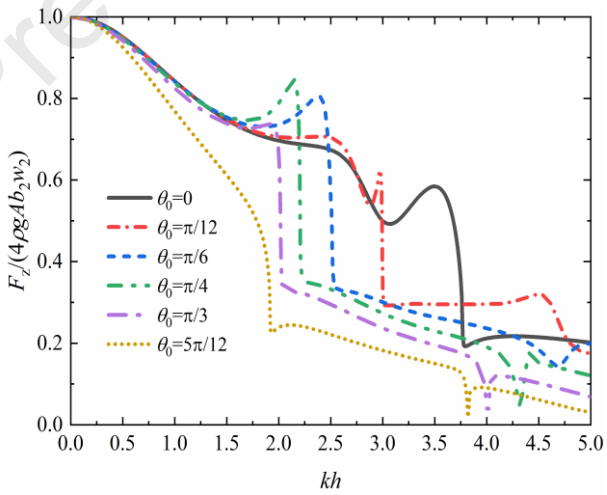

(d) $F_z/(4\rho gAb_2w_2)$

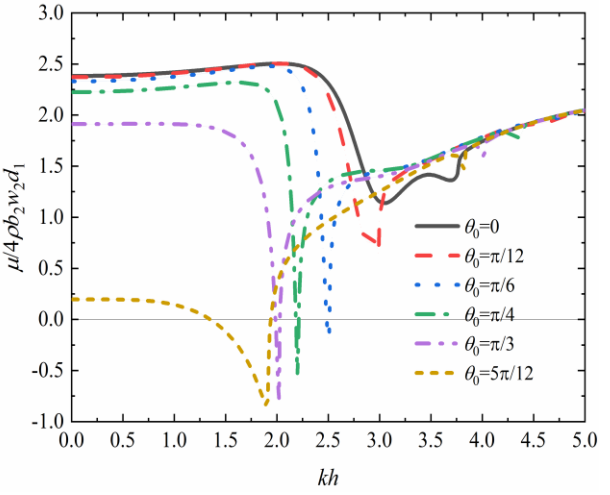

(e) $\mu/(4\rho b_2w_2d_1)$

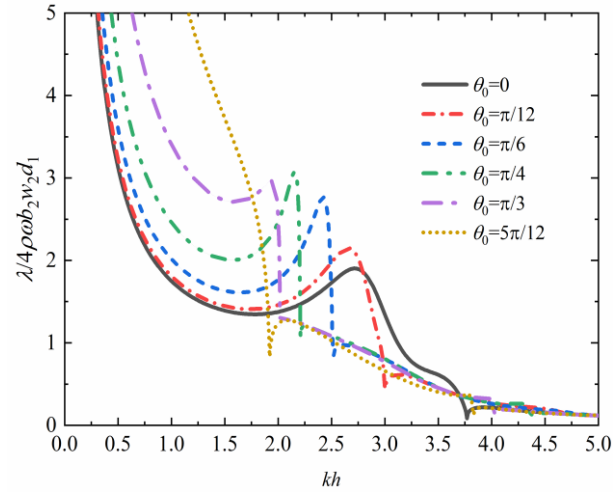

(f) $\lambda/(4\rho\omega b_2w_2d_1)$

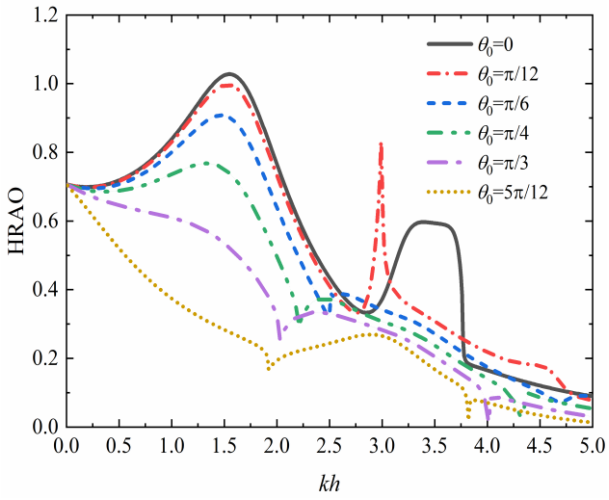

(g) HRAO

Fig. 4. Results of η, K_T, K_R, $F_z/(4\rho g A b_2 w_2)$, $\mu/(4\rho b_2 w_2 d_1)$, $\lambda/(4\rho\omega b_2 w_2 d_1)$ and HRAO for different incident wave angles $\theta_0 = 0$, $\pi/12$, $\pi/6$, $\pi/4$, $\pi/3$, and $5\pi/12$.

Table 1. The *kh* corresponds to the first- and second-order reflected and transmitted propagating waves for different incident angles.

incident angle	0	π/12	π/6	π/4	π/3	5π/12
first-order	3.77	3.00	2.52	2.21	2.02	1.91
second-order	/	/	/	4.41	4.04	3.83

The existence of the periodicity of this system leads to the phenomenon of multiple order reflected and transmitted propagating waves along with the different directions. The trigger wavenumber of this phenomenon is satisfied by $kl = |m\pi/(1 \pm \sin\theta_0)|$ ($m = \pm1, \pm2, \ldots$) accurately, corresponding to Rayleigh wavenumbers (Tokić and Yue, 2019), which results in abrupt changes of hydrodynamic qualities. Therefore, m-th critical wavenumber $(kl)_{(m)}^{cw}$ is found, corresponding to the appearance of m-th order reflected and transmitted propagating waves.

The relative wave amplitude ζ_n/A in the Ω_n ($n = 1, 2, 4, 5$) is expressed as

$$\zeta_n/A = \left|\mathrm{i}\omega\left(\phi_S^{(n)} + \phi_R^{(n)}\right)/(gA)\right|. \tag{35}$$

ζ_1/A at $kh = 1.91$ and 3.83 for $\theta_0 = 5\pi/12$, corresponding to the appearance of the first- and second-order reflected and transmitted propagating wave, is shown in Fig. 5.

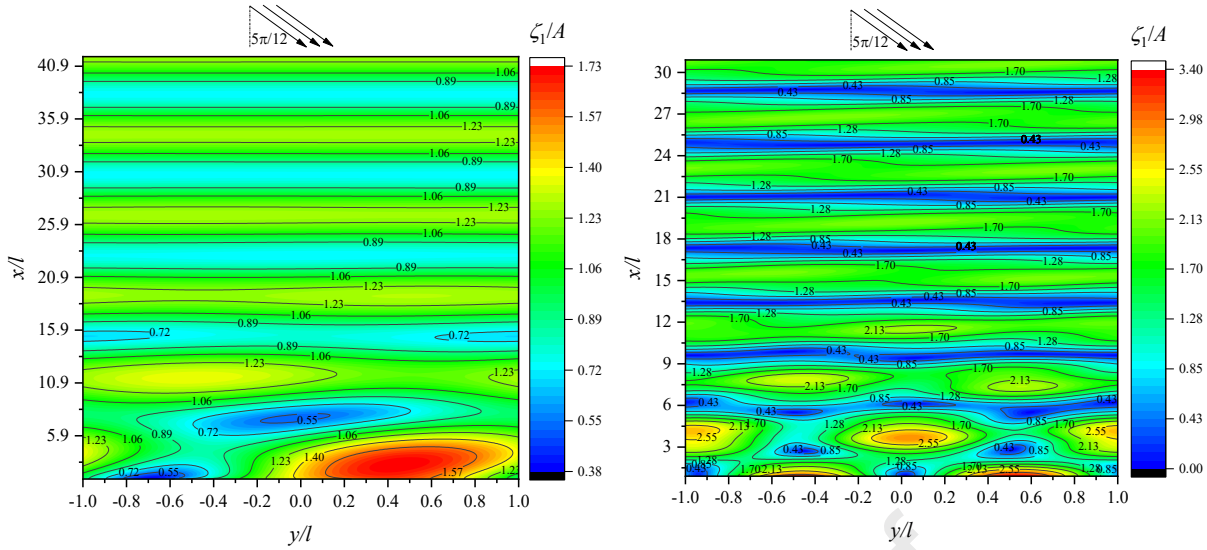

(a) kh = 1.91 (b) kh = 3.83

Fig. 5. ζ_1/A at kh = 1.91 and 3.83 for $\theta_0 = 5\pi/12$.

The maximum ζ_1/A at $(kl)^{cw}_{(2)}$ is greater than that of the $(kl)^{cw}_{(1)}$. The existence of multiple orders reflected and transmitted waves for this integrated system may lead to an increment of K_R and K_T (in Fig. 4b and 4c), i.e., a strong reflection phenomenon. This denotes the wave interference with an identical phase, which may result in a decrease of the incident wave energy transmitted into the wave chamber. Consequently, η, F_z and HRAO are mitigated accompanied by the appearance of first-order reflected and transmitted propagating waves. Besides, there also appear some small valleys of K_R in the higher-frequency region, which satisfies the relation of $kl = 2\pi/(1 + \sin\theta_0)$. And the wave power extraction efficiency is close to zero, corresponding to zeros of F_z and HRAO. As shown in Fig. 4b, the variations of the incident angle affect slightly wave attenuation performance of the breakwater, except for some spiked values at $(kl)^{cw}_{(m)}$ (m = 1, 2). This is to say, the effect of the incidence angle is not beneficial for coastal protection. Compared with normal incident waves (Zhao et al., 2020), the multiple orders propagating waves along different directions have a significant influence on η, instead of y-direction resonance (perpendicular to the incident wave) ($kl = n\pi$, n = 1, 2, …). Under special circumstances, the natural resonance of buoy would be avoided by multiple orders propagating waves (as shown in Fig.4a). However, the y-direction resonance is satisfied perfectly by a special example of $kl = |m\pi/(1 \pm \sin\theta_0)|$ at $\theta_0 = 0$. The latter phenomena are more sensitive to the former in the calculated frequency region. As indicated in Fig. 4e and 4f, the negative added mass emerges (except for 0 and π/12) at the $(kl)^{cw}_{(1)}$. Correspondingly, a sudden reduction of the radiation damping is found.

The radiation damping represents the ability to radiate waves due to the heaving motion of an oscillating buoy, which determines the wave power extraction performance of the devices (Falnes and Kurniawan, 2020). Physically, energy radiated to the far-field decreases, and the absorbed energy of the WEC device is mitigated. However, compared to other incident angles, radiation damping of $\theta_0 = 0$ and $\pi/12$ modifies gently at $(kl)^{cw}_{(1)}$.

For the case of $\theta_0 = \pi/12$, η experiences a dramatic change with a spike value (i.e., 74%) at kh = 2.99 and a valley value (i.e., 35%) at kh = 3.00 shown in Fig. 4a, which is different to other incident wave angles. The corresponding ζ_1/A is shown in Fig. 6. The wave accumulation behavior with a smaller incident angle is achieved, and suddenly more reflected propagating waves carrying wave energy result in a reduction of η. Furthermore, η and F_z for smaller incident wave angles $\theta_0 = \pi/20$, $\pi/15$, $\pi/12$, $\pi/10$, $\pi/8$ and $\pi/7$ were plotted in Fig. 7. There is little distinction among different angles in the region $0 \le kh \le 2.0$. The spiked value decreases with the increasing incident angles, and the wave gathering behavior becomes unsatisfactory, accompanied by the appearance of the first-order reflected and transmitted propagating waves. Compared to the results in Fig. 4a, the spiked value of η vanish for a greater incident angle. This is due to that an increment of F_z also vanishes with the increasing incidence angles when the frequency is close to $(kl)^{cw}_{(1)}$, as indicated in Fig. 7b.

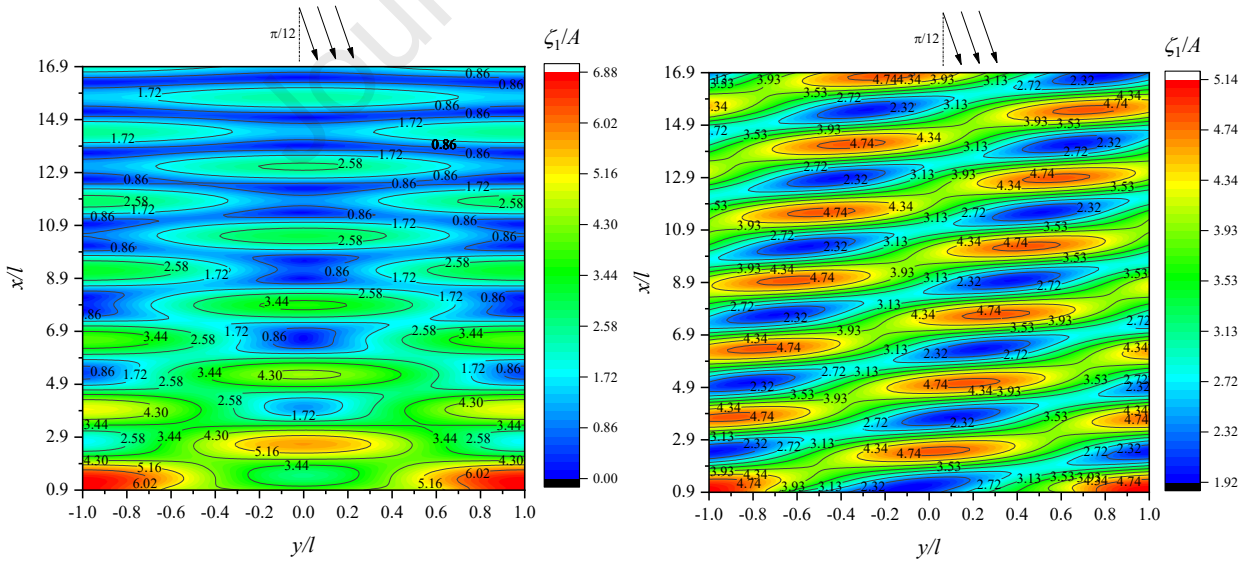

(a) kh = 2.99 (b) kh = 3.00

Fig. 6. ζ_1/A at kh = 2.99 and 3.00 for $\theta_0 = \pi/12$.

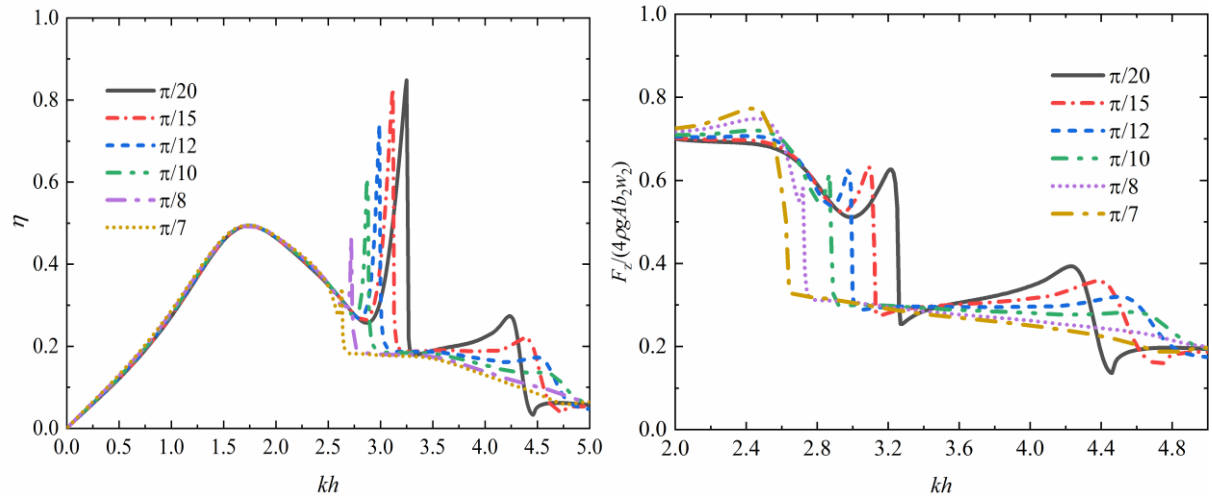

(a) η (b) $F_z/(4\rho gAb_2w_2)$

Fig. 7. Results of η and $F_z/(4\rho gAb_2w_2)$ for different incident wave angles θ_0 = π/20, π/15, π/12, π/10, π/8 and π/7.

We introduce the interaction factor q to evaluate the array effect and the hydrodynamic interactions between the buoy and the caisson, i.e.,

$$q = \frac{P_c}{P_{\text{isolated}}}, \tag{36}$$

where P_c and P_{isloated} represent the power output per unit width of the proposed system and a corresponding 2D heaving rectangular buoy device, respectively. The draft and breadth of the 2D rectangular buoy WEC are identical to that of the proposed system (i.e., d_1 and $2B$, respectively). The optimal PTO damping is used to calculate the extracted power. Fig. 8 plots results of the interaction factor for b_2/h = 0.15 and 0.2. The other wave/geometrical parameters of the proposed system are fixed as l/h = 2/3, B/h = 5/6, d_1/h = 1/3, d_2/h = 11/12, $w_1/h = w_2/h$ = 1/3, $b_1/h = 1 \times 10^{-6}$, and θ_0 = 0. As shown in Fig. 8, two peaks (>1) are observed at the range of $0 < kh < 5.0$, which is corresponding to the trend of the efficiency (see Fig. 4a). $q > 1$ demonstrates the constructive hydrodynamic interaction of the caisson and the buoys. That is to say, even though the size of a buoy is reduced, the constructive hydrodynamic interactions between the buoys and caissons lead to the enhancement of hydrodynamic efficiency. But, a frequency range with $q < 1$ is also observed due to the negative hydrodynamic interactions of the caisson and the buoys.

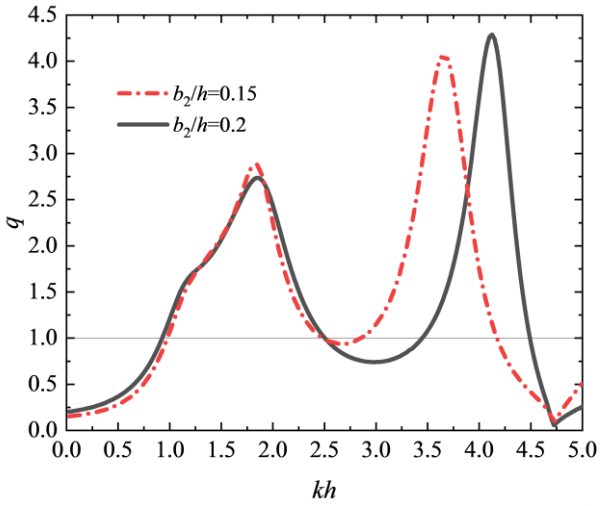

Fig.8. Results of q for b_2/h = 0.15 and 0.2.

Apart from η, wave capture factor $q_c = P_c/P_0$, in which P_0 denotes the power extraction efficiency of the proposed system under the normal incident waves ($\theta_0 = 0$), can be used to evaluate the influence of incident angle on the wave power extraction. Based on the above test cases, the results of q_c for θ_0 = π/12, π/6, π/4, π/3 and 5π/12 are shown in Fig. 9. q_c is equal to 1.0 for $\theta_0 = 0$, not plotted here. A hydrodynamic efficiency equivalent to that under the normal incident waves is obtained for smaller incident angles and in the lower frequency region but decreases considerably with the greater angle at $0 \le kh \le 2.75$. A decline in q_c coincides at $(kl)^{cw}_{(1)}$. But a spiked value for $\theta_0 = \pi/12$ at $kh = 2.99$ is found and the reason is referred to in Fig. 7b.

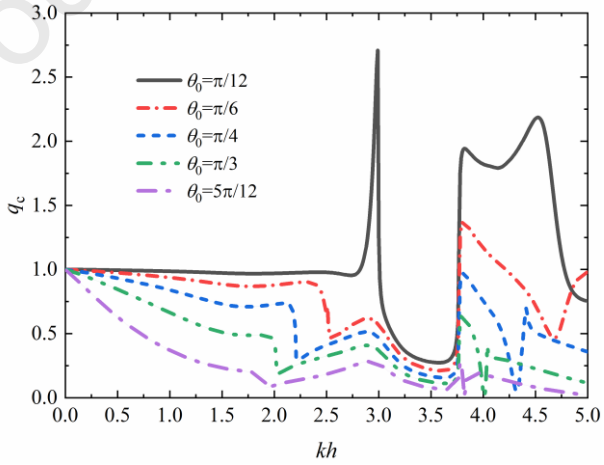

Fig. 9. Results of q_c for θ_0 = π/12, π/6, π/4, π/3 and 5π/12.

4.2 Effect of caisson breadth

The wave/geometry dimensions are set for d_1/h = 1/6, l/h = 1/2, w_1/l = 1/2, w_2/l = 1/2, d_2/h = 0, θ_0 = π/4, b_2/h = 1/3 and $b_1/B = b_3/B$. Each oscillating buoy is arranged in the center of the wave chamber, and the flange is not involved. Fig. 10 shows results of hydrodynamic efficiency η, transmission

coefficients K_T and reflection coefficients K_R for cases of B/h = 2/3, 1, 5/3, and 8/3. Some oscillations of hydrodynamic qualities emerge in the lower-frequency region. The oscillation magnitude is more remarkable with a greater caisson breadth, due to multiple wave resonances inside the wave chamber (Zhao et al., 2020). Interestingly, the maximum of η approaches 50% of the x-direction incident wave energy component. Similar phenomena were also found in Zhao et al. (2020). The maximum hydrodynamic efficiency is not associated with the y-direction component of the incident wave energy. A decline of η for different caisson breadths was found noticeably beyond $(kl)_{(1)}^{cw}$ (i.e., kh = 3.68). K_T also exhibits a fall correspondingly, instead of a spiked value (as is shown in Fig. 4b), which is beneficial for coastal protection. This is due to the that the magnitude of the reflected wave is amplified, corresponding to the strong reflection phenomena (i.e., 0.95).

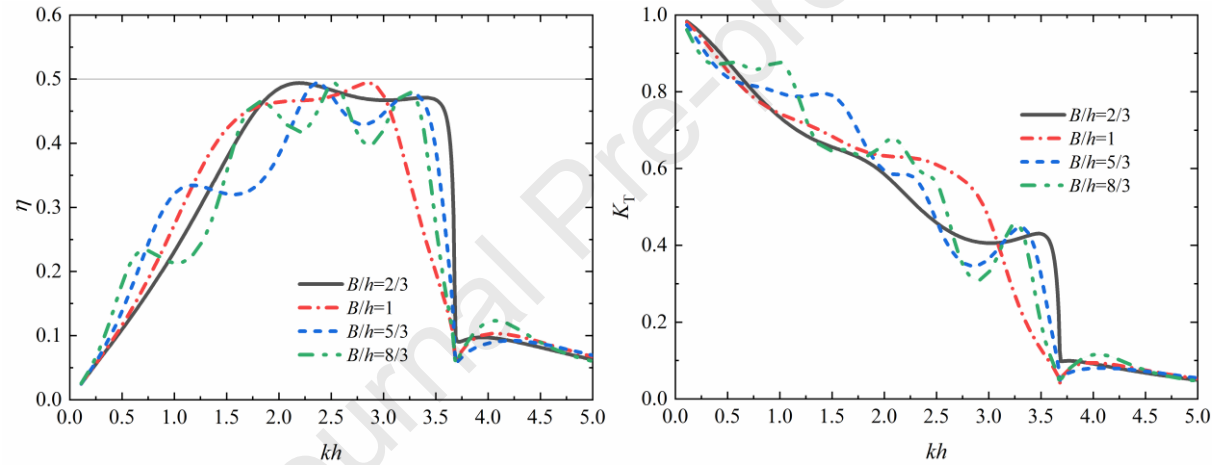

(a) η (b) K_T

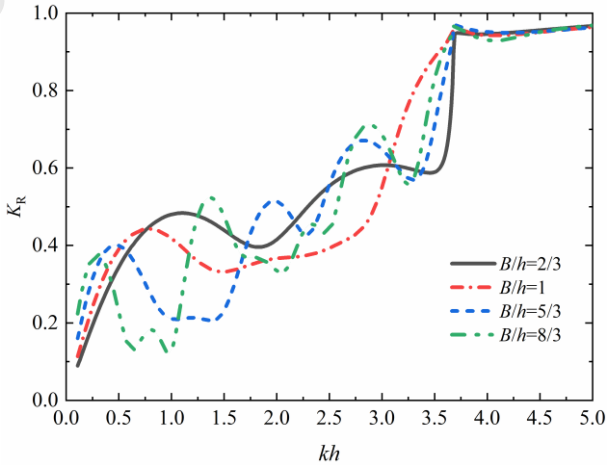

(c) K_R

Fig. 10. The results of η, K_T, and K_R for cases of B/h = 2/3, 1, 5/3, and 8/3.

4.3 Effect of caisson width

The caisson width of breakwater affects significantly the occurrence of multiple orders propagating

waves. The results of η, K_T, K_R, $\mu/(4\rho b_2 w_2 d_1)$, $\lambda/(4\rho\omega b_2 w_2 d_1)$ $F_z/(4\rho g A b_2 w_2)$ and HRAO for w_1/h = 0.4, 1, 1.5 and 2 are shown in Fig. 11. The other parameters are selected for d_1/h = 1/6, w_2/h = 1/2, d_2/h = 1/6, $\theta_0 = \pi/4$, b_2/h = 1/2, B/h = 1 and $b_1/B = b_3/B$. Significant changes in hydrodynamic qualities are found throughout the whole frequency region. η experiences an increasing trend followed by repeated rapid oscillations. This abrupt change corresponds to the occurrence of multiple orders reflected and transmitted propagating waves (i.e., multiple critical wavenumbers), i.e., kh = 2.040 and 4.080 for w_1/h = 0.4; kh = 1.225, 2.450 and 3.670 for w_1/h = 1.0; kh = 0.915, 1.830, 2.745 and 3.661 for w_1/h = 1.5; kh = 0.735, 1.470, 2.205, 2.945 and 3.680 for w_1/h = 2.0. The first peak of η shifts to the lower-frequency region with an increasing caisson width. The presence of first-order propagating waves accounts for a significant role in η and HRAO (as shown in Fig. 11a and 11g), instead of wave resonances inside the wave chamber (Zhao et al., 2020), which is an unwanted result from the perspective of WEC performance. Therefore, the wave power extraction performance of the hybrid breakwater-WEC system is not only dependent on the natural resonance but also on the first-order propagating waves. In general, the presence of the first-order propagating waves dictates the hydrodynamic efficiency of the system. If $(kl)^{cw}_{(1)}$ is dominated in the lower frequency regime, wave power extraction would be compromised at the remaining frequency region. Meanwhile, a greater width significantly hinders the wave power extraction performance (i.e., effective frequency bandwidth). K_R and K_T also exhibit some precipitous modifications. The greater the caisson width is, the greater K_R is and the less K_T is. Therefore, better wave attenuation performance can be achieved, beneficial for coastal defense.

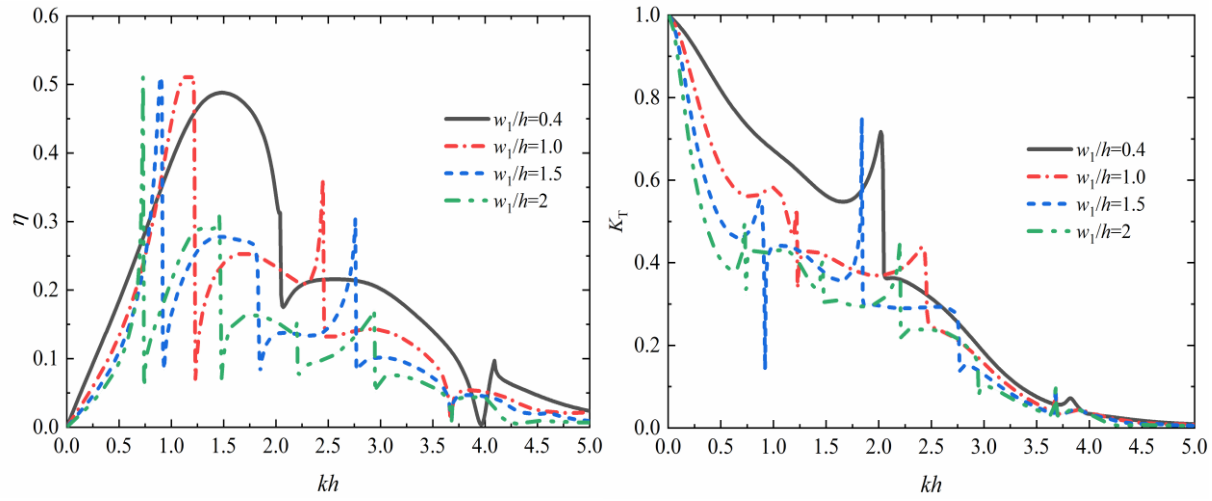

(a) η (b) K_T

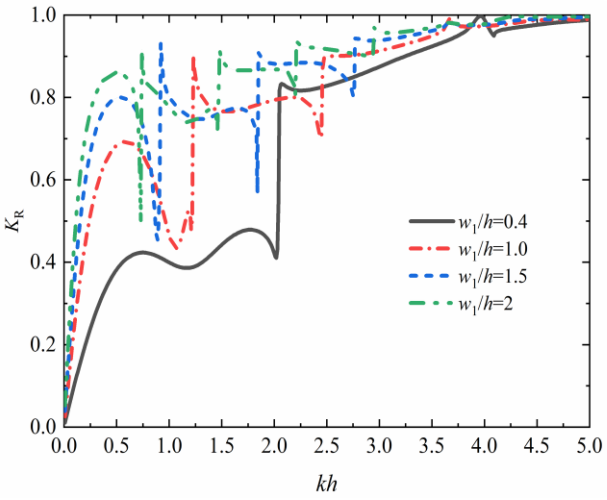

(c) K_R

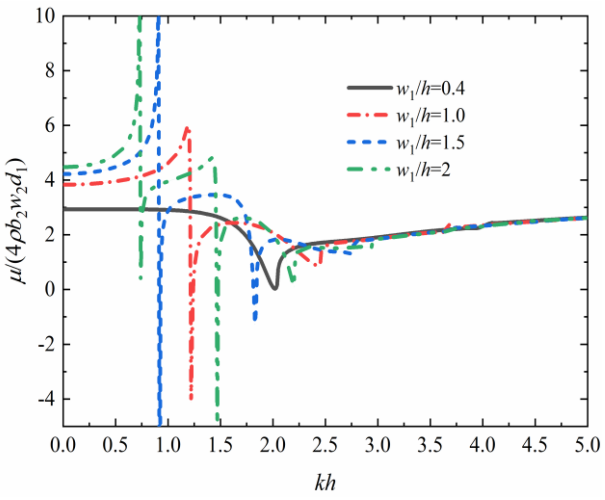

(d) $\mu/(4\rho b_2 w_2 d_1)$

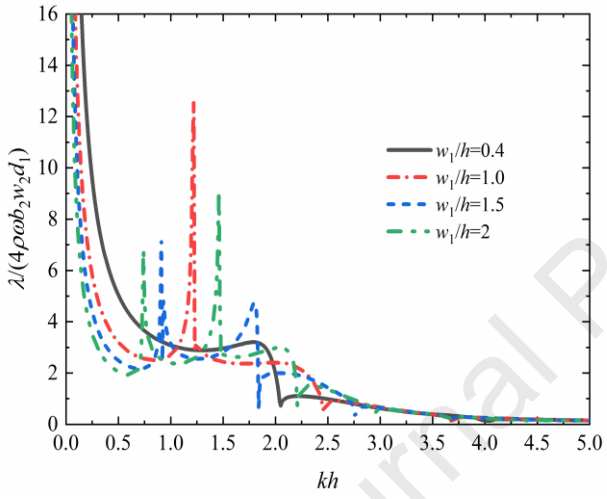

(e) $\lambda/(4\rho\omega b_2 w_2 d_1)$

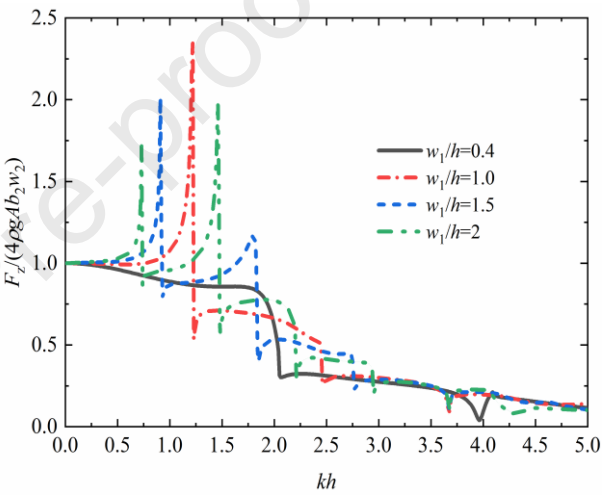

(f) $F_z/(4\rho g A b_2 w_2)$

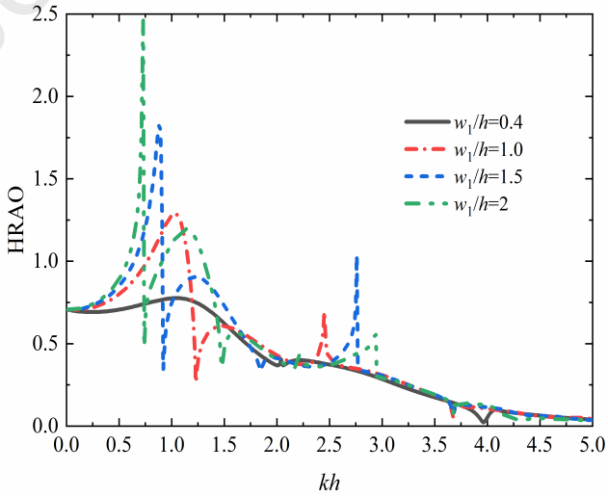

(g) HRAO

Fig. 11. Results of η, K_T, K_R, $\mu/(4\rho b_2 w_2 d_1)$, $\lambda/(4\rho\omega b_2 w_2 d_1)$, $F_z/(4\rho g A b_2 w_2)$ and HRAO for different caisson widths w_1/h = 0.4, 1, 1.5 and 2.

μ and HRAO demonstrate abrupt changes in the lower-frequency region. Correspondingly, a peak

value of λ emerges, and η approaches the first peak value. This phenomenon of wave resonance was reported by Zhang et al. (2020). The variation magnitude of μ, λ, and HRAO is weakened in the higher-frequency region. This is due to that more reflected wave is propagated out of the breakwater, and the wave energy gathering behavior inside the wave chamber is not satisfactory. For the case of w_1/h = 0.4, the wave power extraction efficiency is close to zero at kh = 3.97, corresponding to the zero of F_z and HRAO. Owing to the presence of the flange, a buoy is located at the wave nodes in the confined area by the composition of the incident and reflected waves from the flange, and a detailed explanation will be given in Section 4.4.

4.4 Effect of flange draft

Hydrodynamic coefficients for different flange drafts d_2/h = 1/6, 1/4, 1/3, 1/2, 2/3 and 5/6 are shown in Fig. 12. The other parameters are set for d_1/h = 1/6, l/h = 5/6, w_1/l = 2/5, w_2/l = 3/5, B/h = 1, b_2/B = 1/2, $b_1/B = b_3/B$ = 1/4, $\theta_0 = \pi/4$. The trend of η is similar to that of HRAO. η exhibits two peaks except for the condition of d_2/h = 1/6. A valley value is found between both peaks. Owing to the reflected waves from the flange, η is enhanced significantly. The maximum η approaches 0.9. The flange is considered as a wave-reflecting wall, and wave energy in the wave chamber can be amplified by the composition of the incident and reflected waves (Zheng et al., 2019). The first peak η slightly shifts to the lower-frequency region with an increase in flange draft, accompanied by the occurrence of the negative added mass and significant changes of radiation damping as shown in Fig. 12e and 12f. The ζ_4/A for kh = 1.09 for d_2/h = 5/6 and kh = 1.13 for d_2/h = 2/3 is shown in Fig. 13. But with a greater incident wave angle, the abrupt change of μ modifies softly.

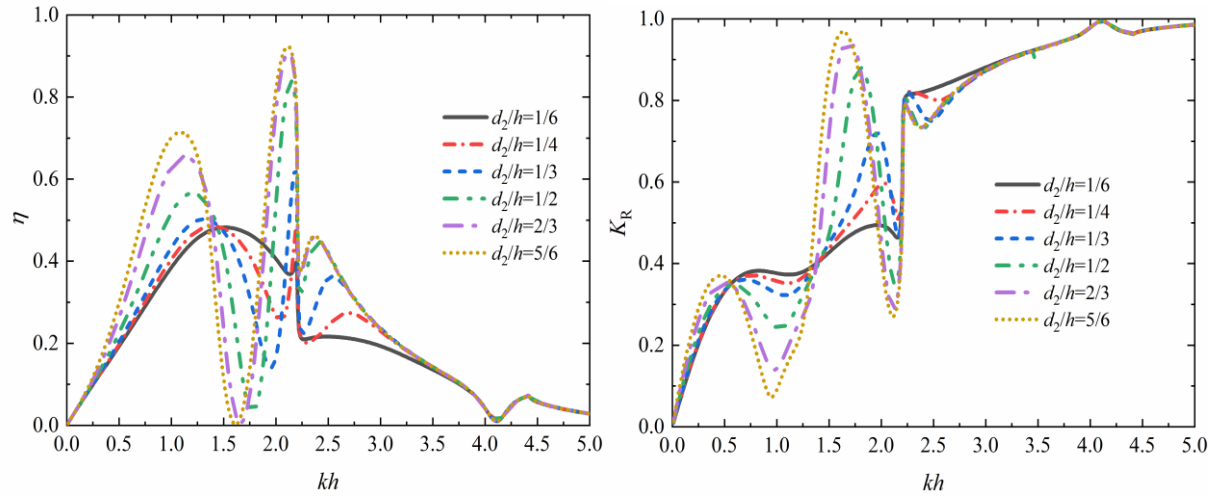

(a) η (b) K_R

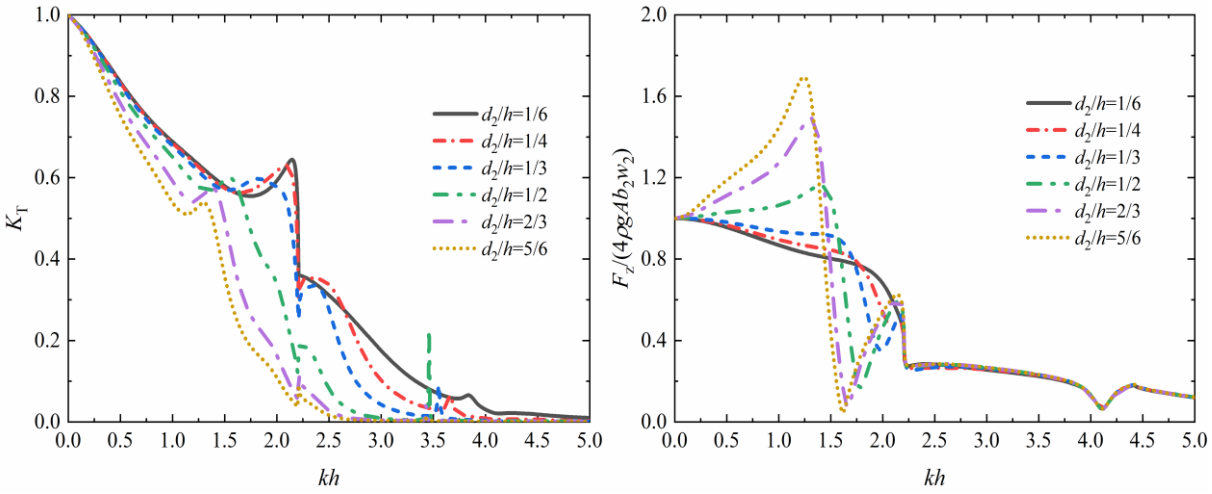

(c) K_T

(d) $F_z/(4\rho gAb_2w_2)$

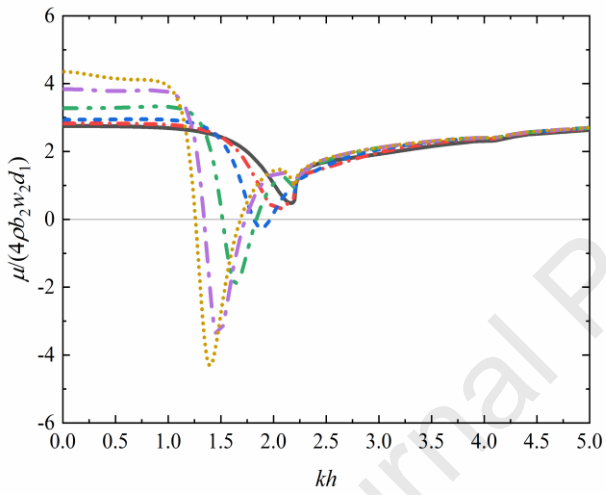

(e) $\mu/(4\rho b_2w_2d_1)$

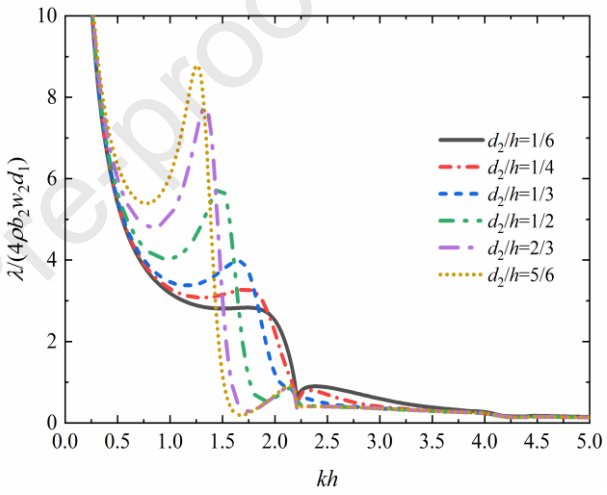

(f) $\lambda/(4\rho\omega b_2w_2d_1)$

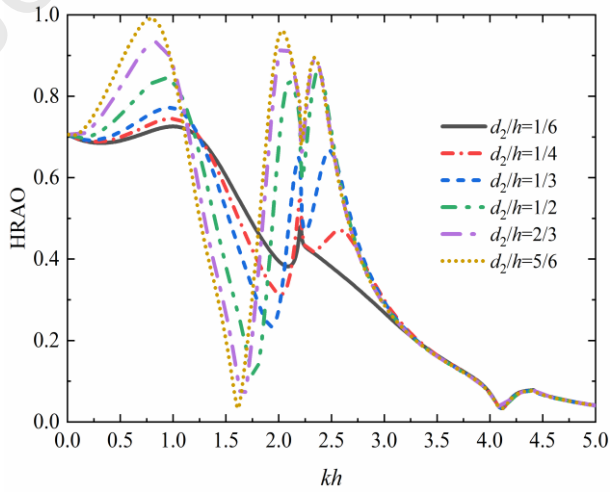

(g) HRAO

Fig. 12. Results of η, K_R, K_T, $F_z/(4\rho gAb_2w_2)$, $\mu/(4\rho b_2w_2d_1)$, $\lambda/(4\rho\omega b_2w_2d_1)$, and HRAO for different flange drafts d_2/h=1/6, 1/4, 1/3, 1/2, 2/3 and 5/6.

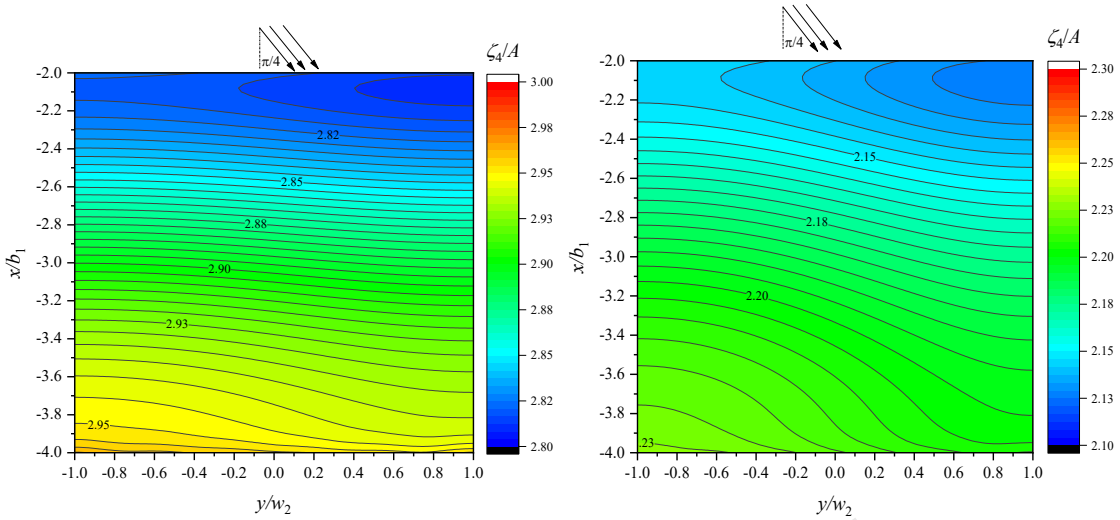

(a) kh = 1.09 for d_2/h = 5/6 (b) kh = 1.13 for d_2/h = 2/3

Fig. 13. The ζ_4/A of the confined area for kh = 1.09 for d_2/h = 5/6 and kh = 1.13 for d_2/h = 2/3.

With an increasing flange draft, the near-standing wave field is formed in the wave chamber. The valley gradually approaches zero owing to the situation where the oscillating buoy may be located in the wave node. A similar phenomenon was found in Zhao et al. (2017; 2019). Correspondingly, F_z and HRAO are closed to zeros, and the buoy remains stationary, which may lead to a strong reflection phenomenon. Interestingly, high hydrodynamic efficiency is found in the $1.8 \leq kh \leq 2.1$. The higher wave power extraction and better wave attenuation performance are achieved for a greater flange draft. With an increasing flange draft, K_T decreases and a little wave is transmitted into the lee side, which considerably prevents the coastline from the wave damage. Therefore, the synergy effect between the breakwater and WECs can be realized simultaneously. However, a reduction of η is also found at $(kl)^{cw}_{(1)}$ (i.e., kh = 2.207). As indicated in Fig. 12, the flange draft is not related to the occurrence of multiple orders propagating waves.

In order to further illustrate the zeros of η, Fig. 14a shows η for different oscillating buoy breadth and d_2/h = 5/6 and $d_1 = 10^{-3}$ (h = 0.6 m). The other geometry is identical to that of Fig. 12. The trigger condition of η = 0 is no different for all cases. Correspondingly, ζ_i/A (i = 2 and 4) for η = 0 at kh = 1.725 are shown in Fig. 14b and 14c, and $b_2 = 10^{-3}$ (i.e., the oscillating buoy is absent) and 10^{-1} (h = 0.6 m) is selected. The standing wave field under the oblique incident waves is formed inside the wave chamber, and an oscillating buoy is located in the wave node (in Fig. 14b). The near-standing wave field is formed with a greater oscillating buoy, as is shown in Fig. 14c.

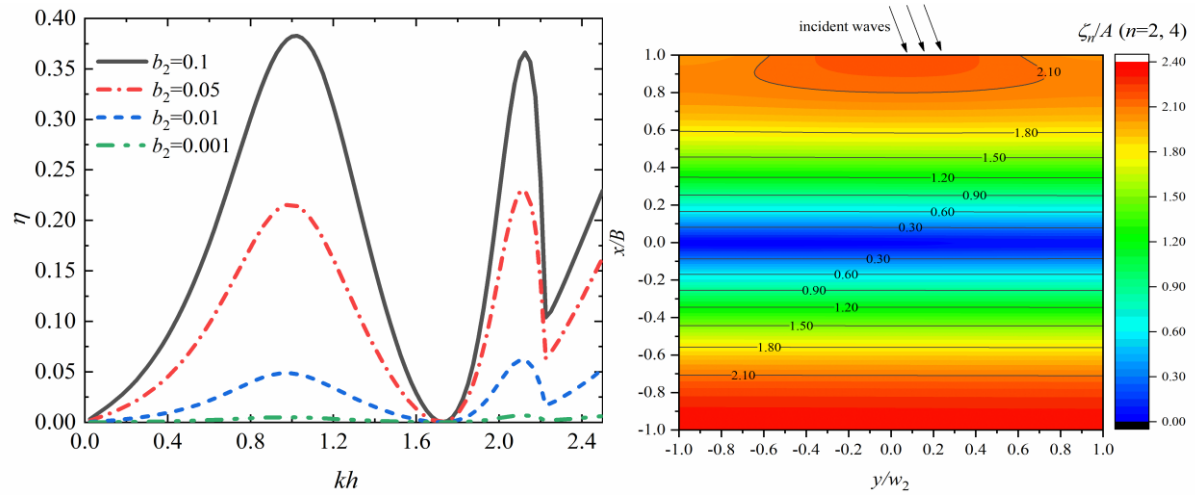

(a) η (b) ζ_n/A for b_2=0.001

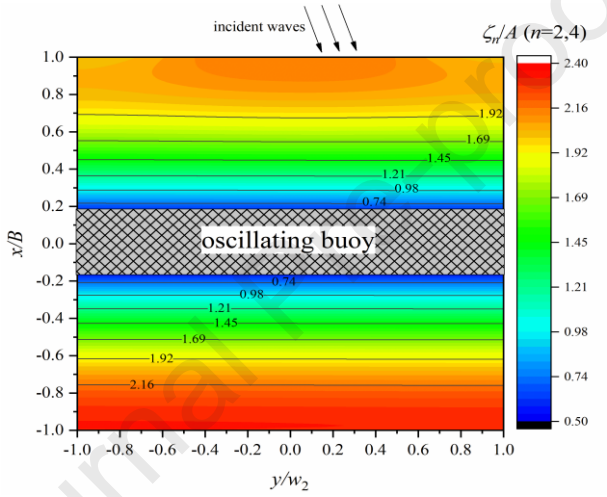

(c) ζ_n/A for b_2=0.1

Fig. 14. (a) η for different buoy breadth; (b) and (c) ζ_n/A for b_2=0.001 and 0.1 (n = 2 and 4).

4.5 Effect of oscillating buoy width

The width of the wave chamber is identical to that of the oscillating buoy. Fig. 15 shows the results of η, K_R, K_T, and HRAO for different buoy widths w_2/h = 1/4, 1/2, 1, 3/2, and 2. The geometry dimensions are selected as d_1/h = 1/6, w_1/h = 1/2, B/h = 1, b_2/B = 1/2, b_1/B = b_3/B = 1/4, θ_0 = π/4, d_2/h = 1/6. Similar to the influence of the caisson width in Section 4.3, abrupt changes of hydrodynamic coefficients are due to the appearance of multiple orders reflected and transmitted propagating waves. The trigger of sudden reduction of hydrodynamic coefficients (i.e., η, K_R, K_T, and HRAO) shifts to the lower-frequency region, with the increasing buoy width. Therefore, the greater width of an oscillating buoy is not beneficial for wave power extraction (η < 0.2). The geometrical configuration of a caisson and an oscillating buoy of width is a key factor to evaluate the hydrodynamic performance of the system. Compared to normal incident waves, the peak of η is substituted for the wave resonance

out of the system due to the first-order propagating waves, as the buoy width increases. To maximize the efficiency, the wave resonance frequency (i.e., natural resonance) inside the wave chamber should occur by avoiding the occurrence of $(kl)_{(1)}^{cw}$. Also, variations of an oscillating buoy width have little effect on the wave attenuation performance, except for some spike values. However, K_R is greater than that of the small oscillating buoy width at $kh > 0.75$. This is due to that more incident wave is reflected with a greater caisson width (i.e., the wave shadowing effect).

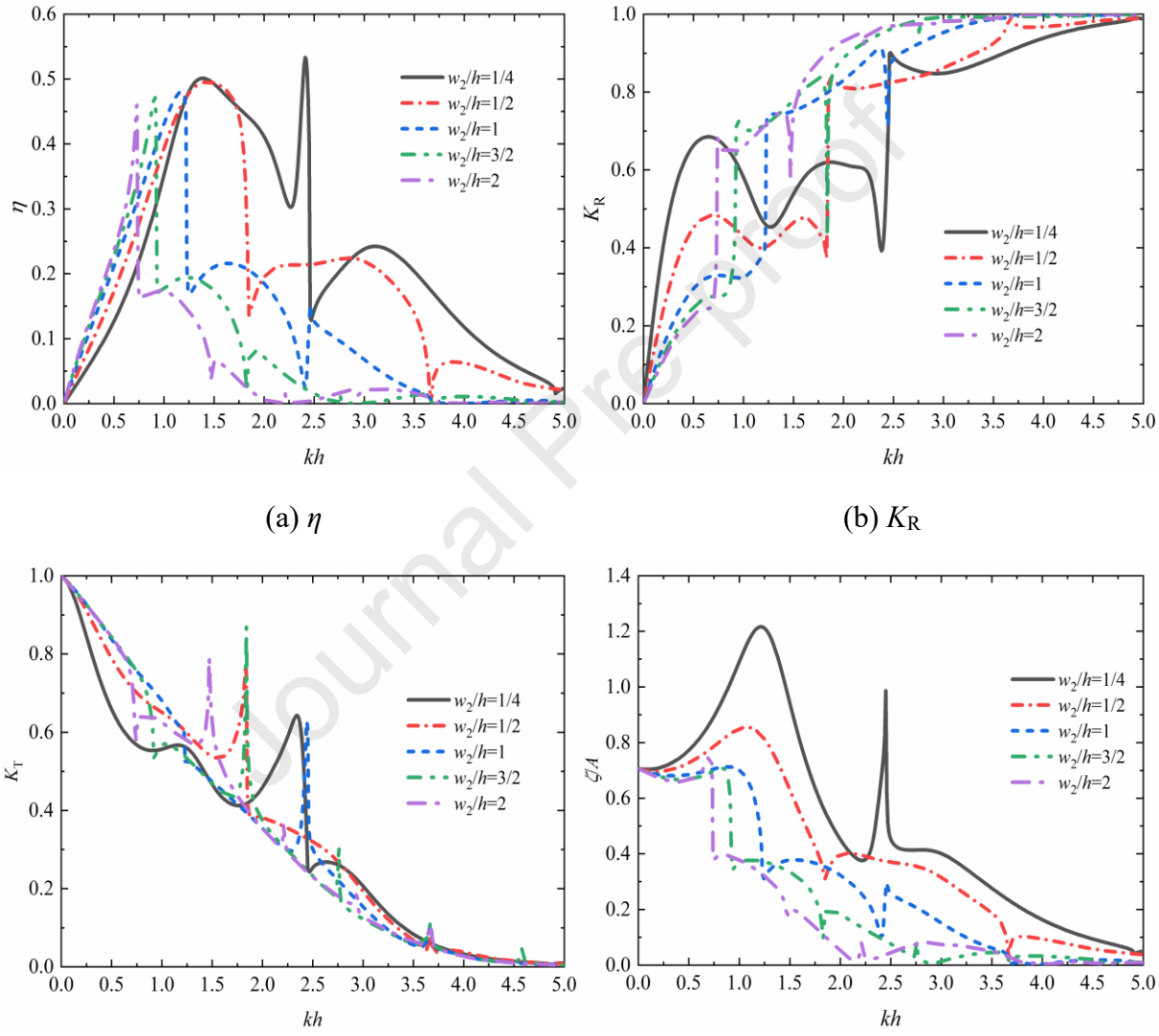

(a) η (b) K_R

(c) K_T (d) HRAO

Fig. 15. Results of η, K_R, K_T, and HRAO for w_2/h = 1/4, 1/2, 1, 3/2, and 2.

4.6 Effect of oscillating buoy breadth

The breadth and draft of 2-D buoy breadth affect significantly the natural frequency, resulting in the frequency of the hydrodynamic efficiency peak value. For this 3-D integrated system, results of hydrodynamic efficiency η and transmission coefficient K_T for different buoy breadths of b_2/B = 1/6,

1/3, 1/2, 2/3, and 5/6 are shown in Fig. 16. The oscillating buoy is located in the center of the wave chamber (i.e., $b_1/B = b_3/B$). The other parameters are set for d_1/h = 1/6, l/h = 5/6, w_1/l = 2/5, w_2/l = 3/5, B/h = 1, $\theta_0 = \pi/4$, d_2/h = 1/6. As indicated in Fig. 16, variations of the oscillating buoy breadth slightly modify the frequency of the natural resonance. An increment of the η is achieved by increasing its breadth. But, the maximum η has a little different for the condition of $b_2/B \geq 1/2$. Especially, when b_2/B = 0.99 (i.e., the wave chamber is filled by an oscillating buoy), η is slightly less than that of b_2/B = 1/2, 2/3, and 5/6. The wave power extraction is also hindered beyond $(kl)^{cw}_{(1)}$. The wave attenuation performance is superior with a greater buoy breadth, which significantly contributes to coastal protection. K_R has an opposite trend to K_T. With an increasing breadth, K_R increases moderately and appears a strong reflection beyond $(kl)^{cw}_{(1)}$. From an engineering perspective, a larger buoy may lead to high construction costs. To realize dual functions of better effective wave power capturing of a device and wave attenuation performance of a breakwater, the optimal geometry of an oscillating buoy may be selected as about b_2/B = 1/2.

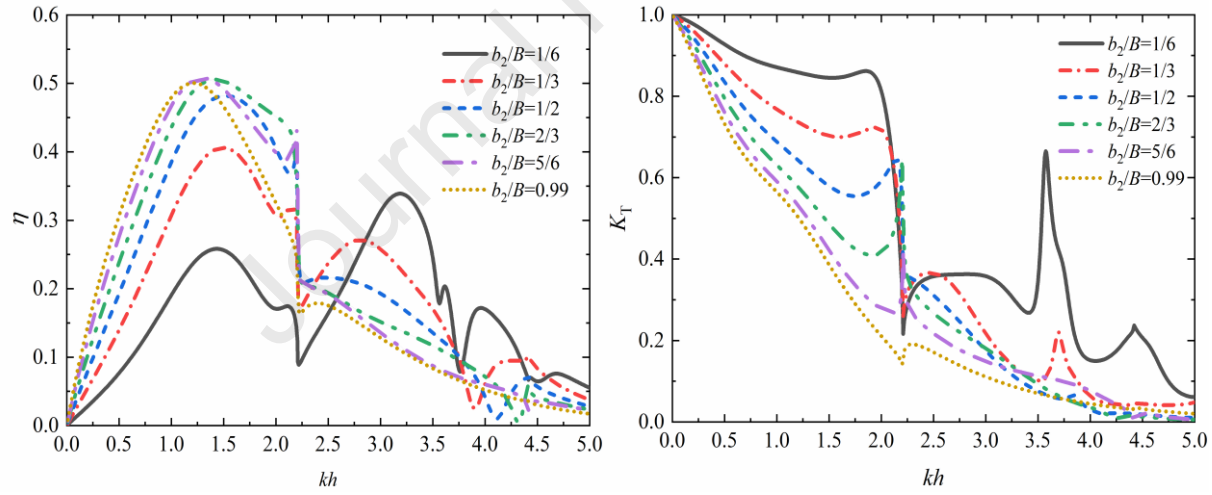

(a) η (b) K_T

Fig. 16. Results of η and K_T for different buoy breadths b_2/B = 1/6, 1/3, 1/2, 2/3, and 5/6.

4.7 Effect of PTO damping

Fig. 17 shows the effect of the PTO damping on the capture width ratio η, transmission coefficient K_T, reflection coefficient K_R and HRAO. The wave and geometrical parameters are set as $d_1/h = d_2/h$ =1/10, l/h = 1/2, w_2/l = 1/2, B/h = 2/5, b_2/B = 1/2, $b_1/B = b_3/B$ = 1/4, and $\theta_0 = \pi/4$. As shown in Fig. 17, η and K_R experience an upward trend with an increasing wavenumber (kh = 1.0, 2.0, and 3.0), but a remarkable reduction of η at kh = 4.0. This is due to that the condition of the kh = 4.0 beyond the

first-order Rayleigh wavenumber leads to an increase in the wave reflection (Fig. 17c). The maximum of η demonstrates $C = 1$ corresponding to the optimal PTO damping, but the valley of K_R is located at $C^{0.5} = 0.5$ nearly. With an increasing PTO damping, K_T and HRAO decrease (in Fig. 17b and 17d), and better wave attenuation performance is realized. Interestingly, the minimum of K_T approaches at $C^{0.5} = 1.5$, instead of $C = 1$.

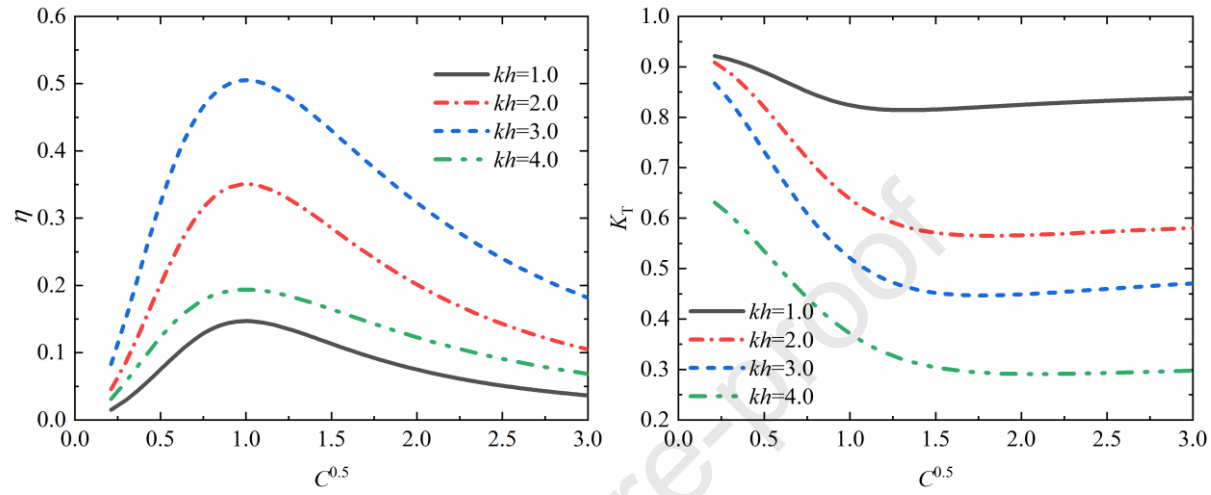

(a) η (b) K_T

(c) K_R (d) HRAO

Fig. 17. Results of η, K_T, K_R, and HRAO versus PTO damping for different dimensionless wavenumber kh = 1.0, 2.0, 3.0, and 4.0 ($\lambda_{PTO} = C \cdot \lambda_{optimal}$).

To illustrate the effect of the PTO damping at the range of $0 < kh < 5.0$, we plotted the results of η and K_T for different PTO damping in Fig. 18. Considering the case of $K_t < 0.5$ and $\eta > 0.2$ as the effective frequency range (Zhao et al., 2019), the available effective frequency region is $1.975 \le kh \le 3.575$, $1.9 \le kh \le 3.575$, $1.675 \le kh \le 3.575$, $1.525 \le kh \le 3.55$, and $1.425 \le kh \le 3.25$ for $\lambda_{PTO} = 0.8\lambda_{optimal}$, $1.0\lambda_{optimal}$, $1.5\lambda_{optimal}$, $2.0\lambda_{optimal}$, and $5.0\lambda_{optimal}$, respectively. The corresponding effective

frequency bandwidths are 1.6, 1.675, 1.9, 2.025, and 1.825. The case of $\lambda_{PTO} = 8.0\lambda_{optimal}$ is neglected due to $\eta < 0.2$. It is concluded that the effective frequency bandwidth is broadened when $\lambda_{PTO} = 2.0$ - $5.0\lambda_{optimal}$, compared to that of $\lambda_{PTO} = 1.0\lambda_{optimal}$.

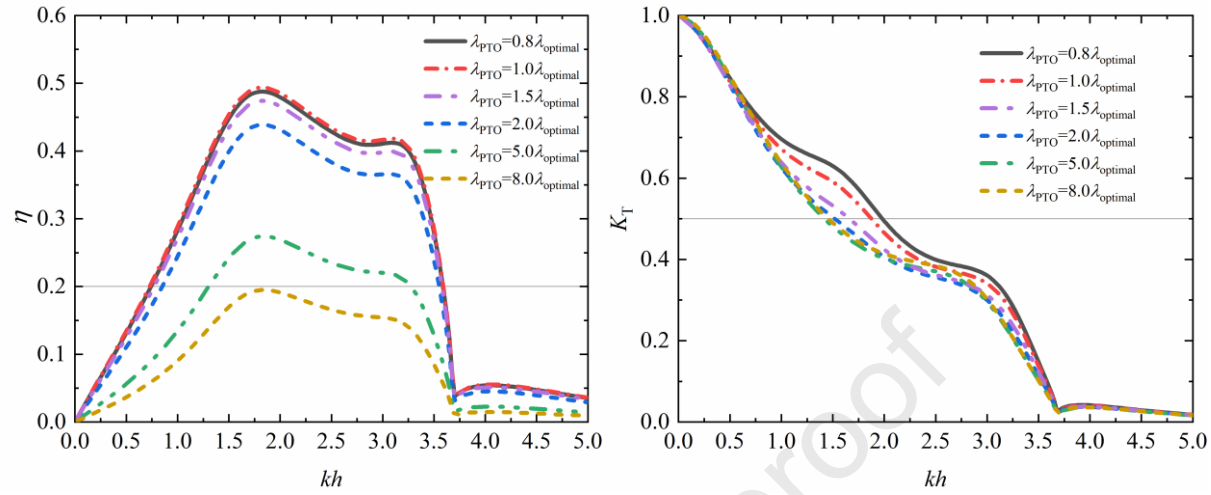

(a)η (b) K_T

Fig. 18. Results of η and K_T for different PTO damping $\lambda_{PTO} = 0.8\lambda_{optimal}$, $1.0\lambda_{optimal}$, $1.5\lambda_{optimal}$, $2.0\lambda_{optimal}$, $5.0\lambda_{optimal}$, and $8.0\lambda_{optimal}$.

5 Further Discussions

In this paper, we investigated the GRP of a periodic array of buoys with a row. Different from an infinite long buoy (Bolton and Ursell, 1973; Zheng et al., 2006; 2007), the flexural propagating waves with a periodicity of array $2l$ along the system were found, which generates oblique waves with periodic distribution due to forced motion of buoys. This assumption has no immediate physical application, but it is easier to compute wave exciting force in the scattering problem, which can agree with generalized wave exciting force deduced from GRP (i.e., Haskind relations). This assumption mainly focuses on the cartesian coordinate system. The incident angle factor can be considered in the velocity potential expressions under the cylindrical coordinate system (Zheng et al., 2019). Therefore, GRP maybe not be involved in the latter coordinate systems.

The caisson array separated by gaps is similar to the diffraction grating in the optics (Wilcox, 1984). The physical phenomenon of the diffraction grating (i.e., Wood anomaly) can be found in the wave interaction with a periodic of caissons (i.e., multiple orders propagating waves) (Wang et al., 2019). Therefore, hydrodynamic coefficients (i.e., reflection and transmission coefficients) are also affected significantly at the m-th critical wavenumbers $(kl)^{cw}_{(m)}$). For the proposed system, a periodic of WECs

are integrated into gaps and the periodicity of the array system is not modified, so radiated waves due to the buoy motion should be taken into consideration. Based on the solution of GRP, a periodic of buoys also results in the appearance of multiple orders propagating waves, and the trigger condition is identical to the wave scattering problem (i.e., $(kl)^{cw}_{(m)}$), which was also found in Tokić and Yue (2019). This solution is also helpful for evaluating a compact array of floating rectangle structures.

For the aspect of water wave interaction with structures, the previous literature not only reveals the influence of multiple orders propagating waves on wave attenuation performance of coastal structures (Wang et al., 2019) but also the evaluation of WECs. Renzi and Dias (2012 and 2013) investigated the influence of the channel sloshing modes on the performance of flap-type wave energy converters under the normal incident waves. The sloshing modes can be clarified for a special case of $(kl)^{cw}_{(m)}$ (θ_0 = 0). Tokić and Yue (2019) also found a striking phenomenon that occurs at isolated wavenumbers in periodic WEC arrays (i.e., Rayleigh-Bloch waves). Therefore, the effect of multiple propagating mode waves on both wave attenuation and energy capture performance of hybrid caisson breakwater-WECs is essential under oblique waves. Compared to the normal incident waves, hydrodynamic efficiency is hindered beyond the first-order critical wavenumber. The $(kl)^{cw}_{(1)}$ with greater incidence angles shifts into the lower frequency region and the most wave energy reflected or transmitted out the system results in a decrease in wave energy gathering, under special circumstances. The positive wave gathering effect on hydrodynamic efficiency and the synergy effect is absent. The multiple orders propagating waves dominate the whole frequency domain, instead of wave power extraction. Therefore, the relationship between the natural resonance of the buoy and the water wave resonance outside the system should be emphasized by adjusting the geometrical configurations properly. In addition, the present work can provide a reference for the assessment of the system in the multi-direction waves.

Comprehensively, these findings of this work can also demonstrate the hydrodynamic synergy effect for a hybrid breakwater-WEC system with a greater flange draft, which can make wave energy technology economically competitive and improve the function of coastal defense simultaneously. The valuable guidance for the practical engineering design has been developed, in response to array configuration and preliminary power prediction of hybrid breakwater-WEC systems in real sea states.

To evaluate the advantages of the proposed system with the potential application of coastal

protection, a comparison of K_R between the proposed system and the novel perforated caisson breakwater (Wang et al., 2021) is shown in Fig. 19a. The difference between both structures is that a perforated wall is substituted for an oscillating buoy WEC device to capture incident wave energy. The size of the caisson and the flange is the same as that in (Wang et al., 2021). The wave/geometrical parameters are as follows: $d_1/h = 1/12$, $d_2/h \approx 1.0$, $l/h = 1/2$, $w_1/l = w_2/l = 1/2$, $B/l = 1/2$, $b_2/B = 1/2$, $b_1/h = 1 \times 10^{-6}$, $\theta_0 = \pi/4$ and $\lambda_{PTO} = \lambda_{optimal}$. From the results described in Fig. 19a, we found that the trend of the presters results is similar to that of Wang et al. (2021). And at the range of $1.5 < kh < 3.5$, the present results are relatively smaller. This means that the wave attenuation performance of the present structures is comparable to that proposed by Wang et al. (2021). In addition, a secondary benefit of wave power extraction is achieved for the present structures.

Besides, a comparison of the power output P_c between the proposed system and a linear periodic array of heaving-oscillating buoy WEC devices is illustrated in Fig. 19b. The parameters are selected for $h = 20$ m, $A = 0.5$ m, $w_2 = b_2 = 1$ m, $w_1/w_2 = 3.0$, $B/w_2 = 2.5$, $b_1/w_2 = 1 \times 10^{-6}$, $d_2 = 0$, $d_1/w_2 = 1/2$, $\theta_0 = 0$ and $\lambda_{PTO} = \lambda_{optimal}$. The displacement of the buoy in the present structure is identical to that of Ning et al. (2020). As indicated in Fig. 19b, a significant increment of P_c between 0.0358 to 0.0622 in the range of kl/π is attributed to the wave gathering behavior of adjacent caissons. But a remarkable reduction was observed beyond $kl/\pi = 1$, due to the presence of the first-order propagating waves.

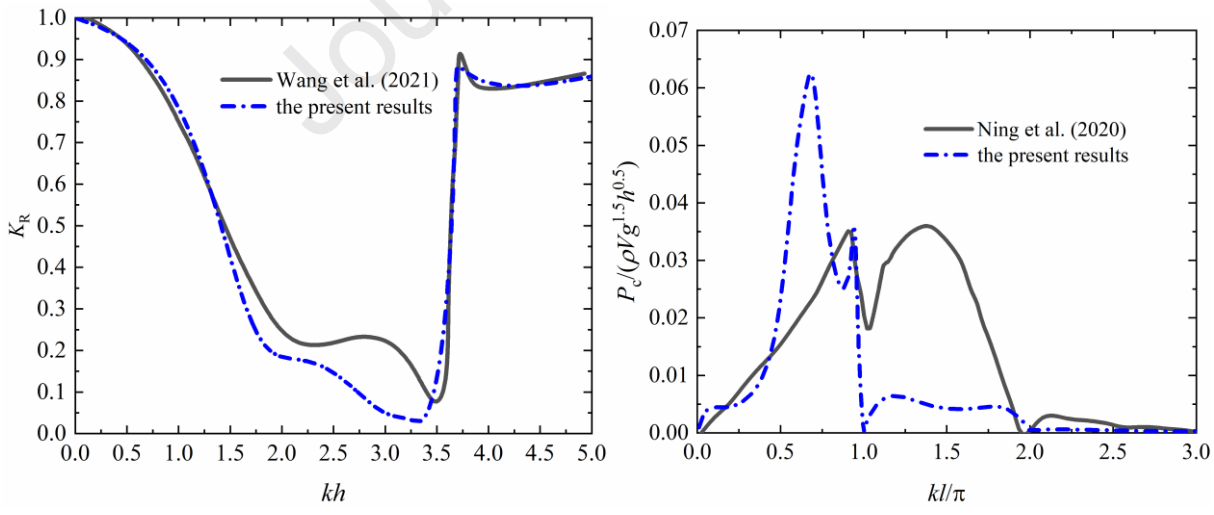

(a) (b)

Fig. 19. Comparison of (a) K_R between the present results and Wang et al. (2021) and (b) $P_c/(\rho V g^{1.5} h^{0.5})$ between the proposed system and Ning et al. (2020). ($V = 4w_2b_2d_1$).

6 Conclusions

In this paper, a 3-D analytical model of oblique wave interaction with a periodic array of oscillating

buoy type wave energy devices embedded in a breakwater was developed, based on the linear potential flow theory and the matching eigenfunction method. The caissons are separated by gaps, and the heaving oscillating-buoy WEC array is arranged in the wave chamber, comprised of adjacent caissons. The linear PTO damping is adapted to convert wave energy to electric power. The generalized radiation problem is considered under oblique waves and validated. Based on pressure and velocity continuity conditions, unknown coefficients of velocity potential expressions can be derived. This theoretical model is ultimately applied to explore the effects of wave/geometrical configurations, and PTO damping. The following conclusions can be drawn:

1) The appearance of multiple-order propagating waves plays a significant role in wave power extraction performance and coastal protection. In particular, the first-order propagating waves were found for a remarkable reduction of η, accompanied by the strong reflection phenomenon. A lower energy capture $q_c < 1$ was found in the lower-frequency region, and the performance mitigation is significant with the increasing incident angle. There are conditions under $q_c > 1$, but they correspond to a low $\eta < 0.2$. Therefore, with a greater incident angle, the wave power extraction is not a dominant role, instead of coastal defense.
2) The influence of caisson width on hydrodynamic qualities is like that of buoy width. Detailly, geometrical configuration modifies the trigger of multiple orders propagating waves. When critical wavenumber is emerged in the low-frequency region, instead of the natural resonance of the buoy, coastal defense is improved significantly, but wave power extraction is hindered. Therefore, the optimal geometry configuration should be designed to avoid the appearance of the first-order critical wavenumber during the effective energy capturing frequency region.
3) The synergy effect (i.e., qualified hydrodynamic efficiency and better wave attenuation) is superior for this proposed integrated system with a greater flange draft. This is due to that the wave energy accumulation in the wave chamber (i.e., reflected waves from the flange) and a little incident wave transmitted into the coastline (i.e., wave shadow effect). However, an oscillating buoy located at the wave node of the standing wave field formed in the confined region may lead to zero hydrodynamic efficiency.

Acknowledgments

The work was supported by the Key Program for International Scientific and Technological Innovation Cooperation between Governments (2019YFE0102500), the National Natural Science

1 Foundation of China (52001086), Basic scientific research business expenses of Central Universities
2 (XK2010021028); China Postdoctoral Science Foundation Funded Project (2019M661257).

Appendix A

The boundary conditions of the scattering problem are as follow:

$$\frac{\partial \phi_S}{\partial z}=0,\ z=-h\ , \tag{A.1}$$

$$\frac{\partial \phi_S}{\partial z}-\frac{\omega^2}{g}\phi_S=0,\ z=0\ , \tag{A.2}$$

$$\frac{\partial \phi_S}{\partial z}=0 \text{ or } \frac{\partial \varphi_R}{\partial z}=1\ ,\ z=-d_1,\ -w_2\le y\le w_2,\ -b_2\le x\le b_2\ , \tag{A.3}$$

$$\frac{\partial \phi_S}{\partial x}=0,\ \text{at } x=r_4 \text{ and } -r_2,\ \left(-l\le y\le -w_2\right)\bigcup\left(w_2\le x\le l\right),\ -h\le z\le 0\ , \tag{A.4}$$

$$\frac{\partial \phi_S}{\partial x}=0,\ \text{at } x=\pm b_2,\ -w_2\le y\le w_2,\ -d_1\le z\le 0\ , \tag{A.5}$$

$$\frac{\partial \phi_S}{\partial y}=0,\ \text{at } y=\pm w_2,\ \begin{cases}\left(-r_2\le x\le -b_2\right)\bigcup\left(b_2\le x\le r_4\right),\ -h\le z\le 0\\ -b_2\le x\le b_2,\ -h\le z\le -d_1\end{cases}, \tag{A.6}$$

$$\frac{\partial \phi_S}{\partial x}=0,\ \text{at } x=-r_2,\ -w_2\le y\le w_2,\ -d_2\le z\le 0\ . \tag{A.7}$$

The coefficients $p_{i,n}$, $\bar{p}_{j,n}$ and $q_{j,n}$ can be expressed as

$$p_{i,n}=\begin{cases}-\sqrt{\lambda_{i,0}},\ \lambda_{i,0}\ge 0,\ n=0,\\ \mathrm{i}\sqrt{-\lambda_{i,0}},\ \lambda_{i,0}<0,\ n=0,\ i=-\infty,...,0,...,+\infty,\\ -\sqrt{\lambda_{i,n}},\ n=1,2,...,\end{cases}\ \begin{cases}\lambda_{i,0}=\gamma_i^2-k^2\\ \lambda_{i,n}=\gamma_i^2+k_n^2\end{cases}\ , \tag{A.8}$$

$$\bar{p}_{j,n}=\begin{cases}\sqrt{\bar{\lambda}_{j,0}},\ \bar{\lambda}_{j,0}>0,\ n=0,\\ \mathrm{i}\sqrt{-\bar{\lambda}_{j,0}},\ \bar{\lambda}_{j,0}\le 0,\ n=0,\ j=0,1,2,...,\\ \sqrt{\bar{\lambda}_{j,n}},\ n=1,2,...,\end{cases}\ \begin{cases}\bar{\lambda}_{j,0}=\bar{\gamma}_j^2-k^2\\ \bar{\lambda}_{j,n}=\bar{\gamma}_j^2+k_n^2\end{cases}\ , \tag{A.9}$$

and

$$q_{j,n}=\sqrt{\bar{\gamma}_j^2+\mu_n^2}\ . \tag{A.10}$$

To derive the unknown coefficients, the conditions of pressure and velocity conditions can be drawn:

1) Pressure continuity conditions ($x = r_4$, b_2, $-b_2$ and $-r_2$):

$$\phi_S^1=\phi_S^2 \text{ and } \varphi_R^1=\varphi_R^2,\ \text{at } x=r_4,\ -w_2\le y\le w_2,\ -h\le z\le 0\ , \tag{A.11}$$

$$\phi_S^2=\phi_S^3 \text{ and } \varphi_R^2=\varphi_R^3,\ \text{at } x=b_2,\ -w_2\le y\le w_2,\ -h\le z\le -d_1\ , \tag{A.12}$$

$$\phi_S^3=\phi_S^4 \text{ and } \varphi_R^3=\varphi_R^4,\ \text{at } x=-b_2,\ -w_2\le y\le w_2,\ -h\le z\le -d_1\ , \tag{A.13}$$

and

$$\phi_S^4 = \phi_S^5 \text{ and } \varphi_R^4 = \varphi_R^5, \text{ at } x = -r_2,\ -w_2 \le y \le w_2,\ -h \le z \le -d_2 \cdot \tag{A.14}$$

2) Velocity continuity conditions ($x = r_4$, b_2, $-b_2$ and $-r_2$):

$$\frac{\partial \phi_S^1}{\partial x} = \begin{cases} \partial \phi_S^2 / \partial x, \\ 0, \end{cases} \text{and } \frac{\partial \varphi_R^1}{\partial x} = \begin{cases} \partial \varphi_R^2 / \partial x, & x = r_4, -w_2 \le y \le w_2,\ -h \le z \le 0 \\ 0, & x = r_4, \left(-l \le y \le -w_2\right) \cup \left(w_2 \le y \le l\right),\ -h \le z \le 0 \end{cases}, \tag{A.15}$$

$$\frac{\partial \phi_S^2}{\partial x} = \begin{cases} \partial \phi_S^3 / \partial x, \\ 0, \end{cases} \text{and } \frac{\partial \varphi_R^2}{\partial x} = \begin{cases} \partial \varphi_R^3 / \partial x, & x = b_2, -w_2 \le y \le w_2,\ -h \le z \le -d_1 \\ 0, & x = b_2, -w_2 \le y \le w_2,\ -d_1 \le z \le 0 \end{cases}, \tag{A.16}$$

$$\frac{\partial \phi_S^4}{\partial x} = \begin{cases} \partial \phi_S^3 / \partial x, \\ 0, \end{cases} \text{and } \frac{\partial \varphi_R^4}{\partial x} = \begin{cases} \partial \varphi_R^3 / \partial x, & x = -b_2, -w_2 \le y \le w_2,\ -h \le z \le -d_1 \\ 0, & x = -b_2, -w_2 \le y \le w_2,\ -d_1 \le z \le 0 \end{cases}, \tag{A.17}$$

$$\frac{\partial \phi_S^4}{\partial x} = \begin{cases} U^{(1)}, \\ 0, \end{cases} \text{and } \frac{\partial \varphi_R^4}{\partial x} = \begin{cases} U^{(2)}, & x = -r_2, -w_2 \le y \le w_2,\ -h \le z \le -d_2 \\ 0, & x = -r_2, -w_2 \le y \le w_2,\ -d_2 \le z \le 0 \end{cases}, \tag{A.18}$$

and

$$\frac{\partial \phi_S^5}{\partial x} = \begin{cases} U^{(1)}, \\ 0, \end{cases} \text{and } \frac{\partial \varphi_R^5}{\partial x} = \begin{cases} U^{(2)}, & x = -r_2, -w_2 \le y \le w_2,\ -h \le z \le -d_2 \\ 0, & x = -r_2, \begin{cases} \left(-l \le y \le -w_2\right) \cup \left(w_2 \le y \le l\right), -h \le z \le 0 \\ -w_2 \le y \le w_2,\ -d_2 \le z \le 0 \end{cases} \end{cases}. \tag{A.19}$$

The function of $U^{(l)}(y,z)$ is written as

$$U^{(l)}(y,z) = \sum_{m=1}^{+\infty} \bar{C}_m(y) \sum_{q=0}^{+\infty} A_{m,q}^{(l)} \frac{2(-1)^q}{\pi \sqrt{\left(h-d_2\right)^2 - \left(z+h\right)^2}} T_{2q}\left(\frac{z+h}{h-d_2}\right), \tag{A.20}$$

where the auxiliary function $U^{(l)}(y,z)$ (l = 1 and 2) was introduced to express the water particle velocities below the flange, $A_{m,q}^{(l)}$ denotes unknown coefficients. Symbolically, $U^{(1)}(y,z)$ and $U^{(2)}(y,z)$ are corresponding to the expressions of scattering and radiation problems, respectively. T_{2q} is the Chebyshev polynomial, and the function of $u_q(z)$ can be expressed as

$$u_q(z) = \frac{2(-1)^q}{\pi \sqrt{\left(h-d_2\right)^2 - \left(z+h\right)^2}} T_{2q}\left(\frac{z+h}{h-d_2}\right). \tag{A.21}$$

The orthogonal relation is satisfied by

$$\int_{-h}^{-d_2} u_q(z) Z_n(z) \mathrm{d}z = \frac{J_{2q}\left\{k_n\left(h-d_2\right)\right\}}{\cos\left[k_n h\right]}, \tag{A.22}$$

where J_{2q} is the Bessel function of order $2q$.

Appendix B

For the wave scattering and radiation problem, a series of linear equations can be written as

$$[\Xi]_{[(10M+Q+9)(N+1)]\times[(10M+Q+9)(N+1)]}[X]_{[(10M+Q+9)(N+1)]\times 1}=\left[\bar{X}\right]_{[(10M+Q+9)(N+1)]\times 1}, \tag{B.1}$$

and

$$[\Xi]_{[(10M+Q+9)(N+1)]\times[(10M+Q+9)(N+1)]}[X']_{[(10M+Q+9)(N+1)]\times 1}=\left[\bar{X}'\right]_{[(10M+Q+9)(N+1)]\times 1}, \tag{B.2}$$

where $[X]$ and $[X']$ correspond to the unknown coefficients of scattering and radiated spatial velocity potential, in addition to $A_{mq}^{(1)}$ and $A_{mq}^{(2)}$. $[\Xi]$ is any matrix, which can be obtained by

$$[\Xi]=\begin{bmatrix}
[\Xi]^{1,1} & [\Xi]^{1,2} & [\Xi]^{1,3} & 0 & 0 & 0 & 0 & 0 & 0\\
[\Xi]^{2,1} & [\Xi]^{2,2} & [\Xi]^{2,3} & 0 & 0 & 0 & 0 & 0 & 0\\
0 & [\Xi]^{3,2} & [\Xi]^{3,3} & [\Xi]^{3,4} & [\Xi]^{3,5} & 0 & 0 & 0 & 0\\
0 & [\Xi]^{4,2} & [\Xi]^{4,3} & [\Xi]^{4,4} & [\Xi]^{4,5} & 0 & 0 & 0 & 0\\
0 & 0 & 0 & [\Xi]^{5,4} & [\Xi]^{5,5} & [\Xi]^{5,6} & [\Xi]^{5,7} & 0 & 0\\
0 & 0 & 0 & [\Xi]^{6,4} & [\Xi]^{6,5} & [\Xi]^{6,6} & [\Xi]^{6,7} & 0 & 0\\
0 & 0 & 0 & 0 & 0 & [\Xi]^{7,6} & [\Xi]^{7,7} & [\Xi]^{7,8} & 0\\
0 & 0 & 0 & 0 & 0 & [\Xi]^{8,6} & [\Xi]^{8,7} & 0 & [\Xi]^{8,9}\\
0 & 0 & 0 & 0 & 0 & 0 & 0 & [\Xi]^{9,8} & [\Xi]^{9,9}
\end{bmatrix}. \tag{B.3}$$

Here, the rows of $[\Xi]^{r,s}$ for r = 1, 3, 4, 5, 6 and 8 are $(M+1)(N+1)$; for r = 2 and 9 are $(2M+1)(N+1)$, for r = 7 is $(Q+1)(N+1)$. The columns of $[\Xi]^{r,s}$ for s = 2, 3, 4, 5, 6 and 7 are $(M+1)(N+1)$; for s = 1 and 8 are $(2M+1)(N+1)$, s = 9 is $(Q+1)(N+1)$. The I and J are set for the rows and columns of each matrix module, i and j represent the rows and columns of each matrix. The detailed expressions of each matrix can be derived from

a) The boundary condition $x = r_4$:

$$[\Xi]_{i,j}^{1,1}=\beta_{J,I}^{(1)}\alpha_{j-(N+1)J-1,i-(N+1)I-1},\ J=0,\ 1,\ ...,\ 2M;\ I=0,\ ...,M, \tag{B.4}$$

$$[\Xi]_{i,j}^{1,2}=[\Xi]_{i,j}^{1,3}=-\bar{\sigma}_{J,I}\alpha_{j-(N+1)J-1,i-(N+1)I-1},\ J,\ I=0,\ ...,M, \tag{B.5}$$

$$[\Xi]_{i,j}^{2,1}=\varepsilon_{J,I}p_{J,j-(N+1)J-1}\alpha_{j-(N+1)J-1,i-(N+1)I-1},\ J,\ I=0,\ 1,\ ...,\ 2M, \tag{B.6}$$

$$[\Xi]_{i,j}^{2,2}=-\beta_{I,J}^{(2)}\bar{p}_{J,j-(N+1)J}\tanh\left[\bar{p}_{J,j-(N+1)J-1}b_3\right]\alpha_{j-(N+1)J-1,i-(N+1)I-1},\ J=0,\ ...,2M;I=0,\ ...,M, \tag{B.7}$$

and

$$[\Xi]_{i,j}^{2,3}=-\beta_{I,J}^{(2)}\bar{p}_{J,j-(N+1)J}\coth\left[\bar{p}_{J,j-(N+1)J-1}b_3\right]\alpha_{j-(N+1)J-1,i-(N+1)I-1},J=0,\ 1,...,2M;I=0,\ ...,M, \tag{B.8}$$

b) The boundary condition $x = b_2$:

$$\left[\Xi\right]_{i,j}^{3,2}=-\left[\Xi\right]_{i,j}^{3,3}\bar{\sigma}_{J,I}\tau_{j-(N+1)J-1,i-(N+1)I-1},\ J,\ I=0,\ ...,M\ , \tag{B.9}$$

$$\left[\Xi\right]_{i,j}^{3,4}=\left[\Xi\right]_{i,j}^{3,5}=-\bar{\sigma}_{J,I}U_{j-(N+1)J-1,i-(N+1)I-1},\ J,\ I=0,\ ...,M\ , \tag{B.10}$$

$$\left[\Xi\right]_{i,j}^{4,2}=-\bar{\sigma}_{J,I}\bar{p}_{J,j-(N+1)J-1}\tanh\left[\bar{p}_{J,j-(N+1)J-1}b_3\right]\alpha_{j-(N+1)J-1,i-(N+1)I-1},\ J,\ I=0,\ ...,M\ , \tag{B.11}$$

$$\left[\Xi\right]^{4,3}=\bar{\sigma}_{J,I}\bar{p}_{J,j-(N+1)J-1}\coth\left[\bar{p}_{J,j-(N+1)J-1}b_3\right]\alpha_{j-(N+1)J-1,i-(N+1)I-1},\ J,\ I=0,\ ...,M\ , \tag{B.12}$$

$$\left[\Xi\right]^{4,4}=\begin{cases}0 & ,J=0,j=1,\ I=0,\ ...,M\\ -\bar{\sigma}_{0,I}q_{0,j-(N+1)J-1}\tanh\left[q_{0,j-(N+1)J-1}b_2\right]\tau_{i-(N+1)I-1,j-(N+1)J-1},\ J=0,\ j\neq 1,\ I=0,\ ...,M\\ -\bar{\sigma}_{J,I}q_{J,j-(N+1)J-1}\tanh\left[q_{J,j-(N+1)J-1}b\right]_2\tau_{i-(N+1)I-1,j-(N+1)J-1},\ J\neq 0,\ I=0,\ ...,M\end{cases}, \tag{B.13}$$

and

$$\left[\Xi\right]^{4,5}=\begin{cases}-\bar{\sigma}_{0,I}\tau_{i-(N+1)I-1,0}/b_2 & ,\ J=0,j=1,\ I=0,\ ...,M\\ -\bar{\sigma}_{0,I}q_{0,j-(N+1)J-1}\coth\left[q_{0,j-(N+1)J-1}b_2\right]\tau_{i-(N+1)I-1,j-(N+1)J-1},\ J=0,\ j\neq 1,\ I=0,\ ...,M\\ -\bar{\sigma}_{J,I}q_{J,j-(N+1)J-1}\coth\left[q_{J,j-(N+1)J-1}b_2\right]\tau_{i-(N+1)I-1,j-(N+1)J-1},\ J\neq 0,\ I=0,\ ...,M\end{cases}, \tag{B.14}$$

c) The boundary condition $x=-b_2$:

$$\left[\Xi\right]_{i,j}^{5,4}=-\left[\Xi\right]_{i,j}^{5,5}=\bar{\sigma}_{J,I}U_{j-(N+1)J-1,i-(N+1)I-1},\ J,\ I=0,\ ...,M\ , \tag{B.15}$$

$$\left[\Xi\right]_{i,j}^{5,6}=\left[\Xi\right]_{i,j}^{5,7}=-\bar{\sigma}_{J,I}\tau_{j-(N+1)J-1,i-(N+1)I-1},\ J,\ I=0,\ ...,M\ , \tag{B.16}$$

$$\left[\Xi\right]_{i,j}^{6,4}=\left[\Xi\right]_{i,j}^{4,4}, \tag{B.17}$$

$$\left[\Xi\right]_{i,j}^{6,5}=-\left[\Xi\right]_{i,j}^{4,5}, \tag{B.18}$$

$$\left[\Xi\right]_{i,j}^{6,6}=-\bar{\sigma}_{J,I}\bar{p}_{J,j-(N+1)J-1}\tanh\left[\bar{p}_{J,j-(N+1)J-1}b_1\right]\alpha_{j-(N+1)J-1,i-(N+1)I-1},\ J,\ I=0,\ ...,M\ , \tag{B.19}$$

and

$$\left[\Xi\right]_{i,j}^{6,7}=-\bar{\sigma}_{J,I}\bar{p}_{J,j-(N+1)J-1}\coth\left[\bar{p}_{J,j-(N+1)J-1}b_1\right]\alpha_{j-(N+1)J-1,i-(N+1)I-1},J,\ I=0,\ ...,M\ , \tag{B.20}$$

d) The boundary condition $x=-r_2$:

$$\left[\Xi\right]_{i,j}^{7,6}=\bar{\sigma}_{J,I}S_{j-(N+1)J-1,i-(N+1)I-1},\ I=0,\ ...,Q;J=0,\ ...,M\ , \tag{B.21}$$

$$\left[\Xi\right]_{i,j}^{7,7}=-\left[\Xi\right]_{i,j}^{7,6}, \tag{B.22}$$

$$\left[\Xi\right]_{i,j}^{7,8}=\beta_{J,I}^{(1)}S_{j-(N+1)J-1,i-(N+1)I-1},\ I=0,\ 1,...,Q;J=0,\ 1,...,\ 2M\ , \tag{B.23}$$

$$\left[\Xi\right]_{i,j}^{8,6}=-\bar{\sigma}_{J,I}\bar{p}_{J,j-(N+1)J-1}\tanh\left[\bar{p}_{J,j-(N+1)J-1}b_1\right]\alpha_{j-(N+1)J-1,i-(N+1)I-1},\ J=0,\ ...,M;I=0,\ ...,M\ , \tag{B.24}$$

$$\left[\Xi\right]_{i,j}^{8,7}=\bar{\sigma}_{J,I}\bar{p}_{J,j-(N+1)J-1}\coth\left[\bar{p}_{J,j-(N+1)J-1}b_1\right]\alpha_{j-(N+1)J-1,i-(N+1)I-1},\ J=0,\ ...,M;I=0,\ ...,M, \tag{B.25}$$

$$\left[\Xi\right]_{i,j}^{8,9}=\bar{\sigma}_{J,I}S_{i-(N+1)I-1,j-(N+1)J-1},\ J=0,\ ...,Q;I=0,\ ...,M, \tag{B.26}$$

$$\left[\Xi\right]_{i.j}^{9,8}=\varepsilon_{J,I}p_{J,j-(N+1)J-1}\alpha_{j-(N+1)J-1,i-(N+1)I-1},\ I,\ J=0,\ ...,2M, \tag{B.27}$$

and

$$\left[\Xi\right]_{i.j}^{9,9}=\beta_{I,J}^{(2)}S_{i-(N+1)I-1,j-(N+1)J-1},\ I=0,\ ...,2M;J=0,\ ...,Q. \tag{B.28}$$

Here, $\left[\Xi\right]_{i,j}^{r,s}$ denotes the element of any matrix, and functions of $\alpha_{n,u}$, $\bar{\sigma}_{j,v}$, $\varepsilon_{i,\delta}$, $\beta_{i,v}^{(1)}$, $\beta_{i,v}^{(2)}$, $\tau_{n,u}$ and $U_{n,u}$ can be obtained by

$$\alpha_{n,u}=\int_{-h}^{0}Z_n\left(z\right)Z_u\left(z\right)\mathrm{d}z=\begin{cases}0 & ,\ n\neq u\\ \dfrac{1}{\cos^2\left[k_nh\right]}\left(\dfrac{h}{2}+\dfrac{\sin\left[2k_nh\right]}{4k_n}\right), & n=u\end{cases}, \tag{B.29}$$

$$\bar{\sigma}_{j,v}=\int_{-w_2}^{w_2}\bar{C}_j\left(y\right)\bar{C}_v\left(y\right)\mathrm{d}y=\begin{cases}2w_2, & j=v=0\\ w_2 & ,\ j=v\neq0\\ 0 & ,\ j\neq v\end{cases}, \tag{B.30}$$

$$\varepsilon_{i,\delta}=\int_{-l}^{l}E_i\left(y\right)E_\delta^*\left(y\right)\mathrm{d}y=\begin{cases}2l, & i\neq\delta\\ 0, & i=\delta\end{cases}, \tag{B.31}$$

$$\beta_{i,v}^{(1)}=\int_{-w_2}^{w_2}E_i\left(y\right)\bar{C}_v\left(y\right)\mathrm{d}y=\begin{cases}2w_2 & ,\ \gamma_i=0,\ v=0\\ -2\mathrm{i}\sinh\left(\mathrm{i}\gamma_iw_2\right)/\gamma_i & ,\ \gamma_i\neq0,\ v=0\\ w_2\mathrm{e}^{\pm\mathrm{i}\bar{\gamma}_vw_2} & ,\ \gamma_i=\pm\bar{\gamma}_v\\ \left[\begin{matrix}\left(1+\left(-1\right)^{v-1}\right)\sin\left(\gamma_iw_2\right)-\\ \mathrm{i}\left(1-\left(-1\right)^{v-1}\right)\cos\left(\gamma_iw_2\right)\end{matrix}\right]\dfrac{\gamma_i}{\left(\gamma_i\right)^2-\left(\bar{\gamma}_v\right)^2} & ,\ \left|\gamma_i\right|\neq\left|\bar{\gamma}_v\right|\end{cases}, \tag{B.32}$$

$$\beta_{i,v}^{(2)}=\int_{-w_2}^{w_2}E_i^*\left(y\right)\bar{C}_v\left(y\right)\mathrm{d}y=\begin{cases}2w_2 & ,\ \gamma_i=0,\ v=0\\ -2\mathrm{i}\sinh\left(\mathrm{i}\gamma_iw_2\right)/\gamma_i & ,\ \gamma_i\neq0,\ v=0\\ w_2\mathrm{e}^{\pm\mathrm{i}\bar{\gamma}_vw_2} & ,\ \gamma_i=\mp\bar{\gamma}_v\\ \left[\begin{matrix}\left(1+\left(-1\right)^{v-1}\right)\sin\left(\gamma_iw_2\right)+\\ \mathrm{i}\left(1-\left(-1\right)^{v-1}\right)\cos\left(\gamma_iw_2\right)\end{matrix}\right]\dfrac{\gamma_i}{\left(\gamma_i\right)^2-\left(\bar{\gamma}_v\right)^2} & ,\ \left|\gamma_i\right|\neq\left|\bar{\gamma}_v\right|\end{cases}, \tag{B.33}$$

$$\tau_{n,u}=\int_{-h}^{-d_1}Z_n\left(z\right)\varphi_u\left(z\right)\mathrm{d}z=\frac{\left(-1\right)^n k_n\sin\left[k_n\left(h-d_1\right)\right]}{\left(k_n^2-\mu_u^2\right)\cos\left(k_nh\right)}, \tag{B.34}$$

and

$$U_{n,u}=\int_{-h}^{-d_1}\varphi_n\left(z\right)\varphi_u\left(z\right)\mathrm{d}z=\begin{cases}h-d_1 & ,\ n=u=0\\ \left(h-d_1\right)/2, & n=u\neq0\\ 0 & ,\ n\neq u\end{cases}. \tag{B.35}$$

For the basic matrix $[\bar{X}]$ and $[\bar{X}']$, the element of $[\bar{X}]_i^r$ and $[\bar{X}']_i^r$ for $r = 1, 2, \ldots, 9$ can be determined by

$$\left[\bar{X}\right]_i^1 = -\beta_{0,I}^{(1)}\alpha_{0,i-(N+1)I-1},\ I = 0,\ ..., M\ , \tag{B.36}$$

$$\left[\bar{X}\right]_i^2 = \mathrm{i}\kappa_x\varepsilon_{0,I}\alpha_{0,i-(N+1)I-1},\ I = -M, ..., 0, ..., M\ , \tag{B.37}$$

$$\left[\bar{X}'\right]_i^3 = \frac{\mathrm{i}\omega}{gA}\bar{\sigma}_{0,I}W_{i-(N+1)I-1},\ I = 0, ..., M\ , \tag{B.38}$$

$$\left[\bar{X}'\right]_i^4 = -\frac{\mathrm{i}\omega}{gA}\frac{b_2}{h-d_1}\bar{\sigma}_{0,I}\tau_{i-(N+1)I-1,1},\ I = 0, ..., M\ , \tag{B.39}$$

$$\left[\bar{X}\right]_i^5 = -\left[\bar{X}\right]_i^3, \tag{B.40}$$

and

$$\left[\bar{X}'\right]_i^6 = \left[\bar{X}'\right]_i^4, \tag{B.41}$$

where the function of W_u denotes

$$W_u = \int_{-h}^{-d_1}\frac{(z+h)^2 - b_2^2}{2(h-d_1)}\varphi_u(z)\mathrm{d}z = \begin{cases}(h-d_1)^2/6 - b_2^2/2, & u = 0\\ (-1)^u/\mu_u^2, & u \neq 0\end{cases}. \tag{B.42}$$

Consequently, the other basic matrix system is the zeros matrix.

References

Abul-Azm, A.G., Gesraha, M.R., 2000. Approximation to the hydrodynamics of floating pontoons under oblique waves. Ocean Engineering. 27(4), 365-384.

Astariz, S., Iglesias, G., 2015. The economics of wave energy: a review. Renewable and Sustainable Energy Reviews. 45, 397-408.

Abanades, J., Greaves, D., Iglesias, G., 2014. Coastal defence through wave farms. Coastal Engineering. 91, 299-307.

Bellew S. 2011. Investigation of the response of groups of wave energy devices. Manchester: University of Manchester.

Bloch, F., 1929. Über Die Quantenmechanik Der Elektronen in Kristallgittern. Zeitschrift für Physik. 52(7-8), 555-600.

Bolton, W.E., Ursell, F., 1973. The wave force on an infinitely long circular cylinder in an oblique sea. Journal of Fluid Mechanics. 57(2), 241-256.

Clément, A., McCullen, P., Falcão, A., Fiorentino, A., Gardner, F., Hammarlund, K., Lemonis, G., Lewis, T., Nielsen, K., Petroncini, S., Pontes, M.T., Schild, P., Sjöström, B.O., Sørensen, H.C., Thorpe, T., 2002. Wave energy in Europe: current status and perspectives. Renewable and Sustainable Energy Reviews. 6(5), 405-431.

Clemente, D., Rosa-Santos, P., Taveira-Pinto, F., 2021. On the potential synergies and applications of wave energy converters: a review. Renewable and Sustainable Energy Reviews. 135, 110162.

Dalrymple, R.A., Martin, P.A., 1990. Wave diffraction through offshore breakwaters. Journal of

Waterway, Port, Coastal and Ocean Engineering. 116(6), 727-741.
Di Lauro, E., Maza, M., Lara, J.L., Losada, I.J., Contestabile, P., Vicinanza, D., 2020. Advantages of an innovative vertical breakwater with an overtopping wave energy converter. Coastal Engineering. 159, 103713.
Evans, D.V., 1976. A theory for wave-power absorption by oscillating bodies. Journal of Fluid Mechanics. 77(1), 1-25.
Evans, D.V., Porter, R., 1995. Complementary approximations to wave scattering by vertical barriers. Journal of Fluid Mechanics. 294, 155-180.
Falcão, A.F.D.O., 2010. Wave energy utilization: a review of the technologies. Renewable and Sustainable Energy Reviews. 14(3), 899-918.
Falnes, J., Budal, K., 1982. Wave-power absorption by parallel rows of interacting oscillating bodies. Applied Ocean Research. 4(4), 194-207.
Falnes, J., Kurniawan A. 2020. Ocean waves and oscillating systems: linear interactions including wave-energy extraction. Cambridge University Press.
Garnaud, X., Mei, C.C., 2009. Wave-power extraction by a compact array of buoys. Journal of Fluid Mechanics. 635, 389-413.
Garnaud, X., Mei, C.C., 2010. Comparison of wave power extraction by a compact array of small buoys and by a large buoy. IET Renewable Power Generation. 4(6), 519-530.
He, F., Zhang, H., Zhao, J., Zheng, S., Iglesias, G., 2019. Hydrodynamic performance of a pile-supported OWC breakwater: An Analytical Study. Applied Ocean Research. 88, 326-340.
Islam, H., Mohapatra, S.C., Gadelho, J., Guedes Soares, C., 2019. OpenFOAM analysis of the wave radiation by a box-type floating structure. Ocean Engineering. 193, 106532.
Jalón, M.L., Lira-Loarca, A., Baquerizo, A., Losada, M.Á., 2019. An analytical model for oblique wave interaction with a partially reflective harbor structure. Coastal Engineering. 143, 38-49.
Linton, C.M., McIver, P., 2001. Handbook of Mathematical Techniques for Wave/Structure Interactions, CRC Press.
Liu, Y., Li, Y.C., Teng, B., 2007. The reflection of oblique waves by an infinite number of partially perforated caissons. Ocean Engineering. 34(14-15), 1965-1976.
López, I., Andreu, J., Ceballos, S., Martínez De Alegría, I., Kortabarria, I., 2013. Review of wave energy technologies and the necessary power-equipment. Renewable and Sustainable Energy Reviews. 27, 413-434.
Maradudin, A.A., Simonsen, I., Polanco, J., Fitzgerald, R.M., 2016. Rayleigh and wood anomalies in the diffraction of light from a perfectly conducting reflection grating. Journal of Optics (United Kingdom). 18(2), 024004.
Martins-Rivas, H., Mei, C.C., 2009a. Wave power extraction from an oscillating water column at the tip of a breakwater. Journal of Fluid Mechanics. 626, 395-414.
Martins-rivas, H., Mei, C.C., 2009b. Wave power extraction from an oscillating water column along a straight coast. Ocean Engineering. 36(6-7), 426-433.
Malmo, O., Reitan, A., 1985. Wave-power absorption by an oscillating water column in a channel. Journal of Fluid Mechanics. 158, 153-175.
Mendoza, E., Silva, R., Zanuttigh, B., Angelelli, E., Lykke Andersen, T., Martinelli, L., Nørgaard, J.Q.H., Ruol, P., 2014. Beach response to wave energy converter farms acting as coastal defence. Coastal Engineering. 87, 97-111.
Mustapa, M.A., Yaakob, O.B., Ahmed, Y.M., Rheem, C.K., Koh, K.K., Adnan, F.A., 2017. Wave

energy device and breakwater integration: a review. Renewable and Sustainable Energy Reviews. 77, 43-58.
Nazarov, S.A., Videman, J.H., 2010. Existence of edge waves along three-dimensional periodic structures. Journal of Fluid Mechanics. 659, 225-246.
Ning, D., He, Z., Gou, Y., Göteman, M., 2020. Near trapping effect on wave-power extraction by linear periodic arrays. Sustainability (Switzerland). 12(1), 29.
Politis, C.G., Papalexandris, M.V., Athanassoulis, G.A., 2002. A boundary integral equation method for oblique water-wave scattering by cylinders governed by the modified Helmholtz equation. Applied Ocean Research. 24(4), 215-233.
Renzi, E., Dias, F., 2012. Resonant behaviour of an oscillating wave energy converter in a channel. Journal of Fluid Mechanics. 701, 482-510.
Renzi, E., Abdolali, A., Bellotti, G., Dias, F., 2013. Wave-power absorption from a finite array of oscillating wave surge converters. Renewable Energy. 63, 55-68.
Renzi, E., Dias, F., 2013. Relations for a periodic array of flap-type wave energy converters. Applied Ocean Research. 39, 31-39.
Sannasiraj, S.A., Sundaravadivelu, R., Sundar, V., 2001. Diffraction-radiation of multiple floating structures in directional waves. Ocean Engineering. 28(2), 201-234.
Siddorn, P., Eatock Taylor, R., 2008. Diffraction and independent radiation by an array of floating cylinders. Ocean Engineering. 35(13), 1289-1303.
Simon, M.J., 1982. Multiple scattering in arrays of axisymmetric wave-energy devices. part 1. a matrix method using a plane-wave approximation. Journal of Fluid Mechanics. 120, 1-25.
Strutt, J.W., 1907. On the dynamical theory of gratings. Proceedings of the Royal Society of London. Series A, Containing Papers of a Mathematical and Physical Character. 79(532), 399-416.
Tay, Z.Y., Venugopal, V., 2019. The impact of energy extraction of wave energy converter arrays on wave climate under multi-directional seas. Journal of Ocean Engineering and Marine Energy. 5(1), 51-72.
Teng, B., Zhang, X.T., Ning, D.Z., 2004. Interaction of oblique waves with infinite number of perforated caissons. Ocean Engineering. 31(5-6), 615-632.
Tokić, G., Yue, D.K.P., 2019. Hydrodynamics of periodic wave energy converter arrays. Journal of Fluid Mechanics. 862, 34-74.
Vicinanza, D., Contestabile, P., Quvang Harck Nørgaard, J., Lykke Andersen, T., 2014. Innovative rubble mound breakwaters for overtopping wave energy conversion. Coastal Engineering. 88, 154-170.
Wang, X., Liu, Y., Lu, L., 2019. Analytical solution of oblique wave interacting with a periodic array of specific caissons connected with partially immersed thin walls (comb-type). Ocean Engineering. 186, 106107.
Wang, X.Y., Liu, Y., Lu, L., 2021. Analysis of oblique wave interaction with perforated caisson breakwaters with partial wave absorption parts. Ocean Engineering. 241, 110018.
Wilcox, C.H., 1984. Scattering theory for diffraction gratings. Mathematical Methods in the Applied Sciences. Springer-Verlag New York Inc.
Wolgamot, H.A., Eatock Taylor, R., Taylor, P.H., 2015. Radiation, trapping and near-trapping in arrays of floating truncated cylinders. Journal of Engineering Mathematics. 91(1), 17-35.
Wood, R.W., 1901. On a remarkable case of uneven distribution of light in a diffraction grating spectrum. Proceedings of the Physical Society of London. 18(1), 269-275.

Zhang, Y., Li, M., Zhao, X., Chen, L., 2020. The effect of the coastal reflection on the performance of a floating breakwater-WEC system. Applied Ocean Research. 100, 102117.

Zhang, H., Zhou, B., Vogel, C., Willden, R., Zang, J., Geng, J., 2020. Hydrodynamic performance of a dual-floater hybrid system combining a floating breakwater and an oscillating-buoy type wave energy converter. Applied Energy. 259, 114212.

Zhang Y., Zhao X.L., Geng J., Tao L.B. 2021, A novel concept for reducing wave reflection from OWC structures with application of harbor agitation mitigation/coastal protection: Theoretical investigations. Ocean Engineering, 242, 110075.

Zhao, X., Zhang, Y., Li, M., Johanning, L., 2020. Hydrodynamic performance of a comb-type breakwater-WEC system: an analytical study. Renewable Energy. 159, 33-49.

Zhao, X., Zhang, Y., Li, M., Johanning, L., 2021. Experimental and analytical investigation on hydrodynamic performance of the comb-type breakwater-wave energy converter system with a flange. Renewable Energy. 172, 392-407.

Zhao, X.L., Ning, D.Z., Zou, Q.P., Qiao, D.S., Cai, S.Q., 2019. Hybrid floating breakwater-WEC system: a review. Ocean Engineering. 186, 106126.

Zhao, X., Ning, D., Zhang, C., Liu, Y., Kang, H., Gendelman, O.V., 2017. Analytical study on an oscillating buoy wave energy converter integrated into a fixed box-type breakwater. Mathematical Problems in Engineering. 2017, 3960401.

Zhao, X., Xue, R., Geng, J., Göteman, M., 2021. Analytical investigation on the hydrodynamic performance of a multi-pontoon breakwater-WEC System. Ocean Engineering. 220, 108394.

Zhao, X., Ning, D., Zhang, C., Kang, H., 2017. Hydrodynamic investigation of an oscillating buoy wave energy converter integrated into a pile-restrained floating breakwater. Energies. 10(5), 712.

Zheng, S., Antonini, A., Zhang, Y., Greaves, D., Miles, J., Iglesias, G., 2019. Wave power extraction from multiple oscillating water columns along a straight coast. Journal of Fluid Mechanics. 878, 445-480.

Zheng, Y.H., Shen, Y.M., You, Y.G., Wu, B.J., Jie, D.S., 2006. Wave radiation by a floating rectangular structure in oblique seas. Ocean Engineering. 33(1), 59-81.

Zheng, Y.H., Liu, P.F., Shen, Y.M., Wu, B.J., Sheng, S.W., 2007. On the radiation and diffraction of linear water waves by an infinitely long rectangular structure submerged in oblique seas. Ocean Engineering. 34(3-4), 436-450.

Zhu, D.T., Wang, X.G., Liu, Q.J., 2017. Conditions and phase shift of fluid resonance in narrow gaps of bottom-mounted caissons. China Ocean Engineering. 31(6), 724-735.

Declaration of interests

☒ The authors declare that they have no known competing financial interests or personal relationships that could have appeared to influence the work reported in this paper.

☐The authors declare the following financial interests/personal relationships which may be considered as potential competing interests: